Phase-field lattice Boltzmann modeling of boiling using a sharp-interface energy solver

Mahmood Mohammadi-Shad and Taehun Lee

Phys. Rev. E **96**, 013306 — Published 11 July 2017

DOI: 10.1103/PhysRevE.96.013306

Phase Field Lattice Boltzmann Modeling of Boiling Using a Sharp Interface Energy Solver

Mahmood Mohammadi-Shad and Taehun Lee*

Department of Mechanical Engineering,

City College of City University of New York, New York 10031, USA

Abstract

The main objective of this paper is to extend an isothermal incompressible two-phase lattice Boltzmann equation method to model liquid-vapor phase change problems using a sharp interface energy solver. Two discrete particle distribution functions, one for the continuity equation and the other for the pressure evolution and momentum equations, are considered in the current model. The sharp interface macroscopic internal energy equation is discretized with an isotropic finite difference method to find temperature distribution in the system. The mass flow generated at liquid-vapor phase interface is embedded in the pressure evolution equation. The sharp interface treatment of internal energy equation helps to find the interfacial mass flow rate accurately where no free parameter is needed in the calculations. The proposed model is verified against available theoretical solutions of the two-phase Stefan problem and the two-phase sucking interface problem, with which our simulation results are in good agreement. The liquid droplet evaporation in a superheated vapor, the vapor bubble growth in a superheated liquid, and the vapor bubble rising in a superheated liquid are analyzed and underlying physical characteristics are discussed in detail. The model is successfully tested for the liquid-vapor phase change with large density ratio up to 1000.

PACS numbers: 47.11.j, 47.55.t, 64.70.fm, 44.35.+c

Keywords: Lattice Boltzmann Method, Phase Change, Heat Transfer

* thlee@ccny.cuny.edu

I. INTRODUCTION

The heat transfer mechanisms involving the liquid-vapor phase change provide ample cooling for many industrial application because of the considerable heat transfer associated with the latent heat of the liquid [1]. Liquid-vapor phase change characteristics have been extensively investigated theoretically, numerically, and experimentally by many researchers. By using numerical tools, the phenomena that are difficult to observe experimentally due to complicated physical processes during boiling such as very small spatial scales and fast temporal changes can be successfully studied. A fully detailed numerical simulation of liquid-vapor phase change can be achieved by simultaneously coupling many physical effects none of which can be ignored. The mass, momentum, and energy conservation equations must incorporate the effects of surface tension, latent heat, interfacial mass flow rate, abrupt change of material properties, and phase interface dynamics. One of the most challenging problems in numerical simulations of liquid-vapor phase change is accurate representation of the motion of the phase interface in the presence of phase change.

Numerical simulation of boiling has been carried out using sharp interface and diffuse interface techniques. In the sharp interface approach, liquid-vapor phase change has been simulated with front tracking method [2], Volume of Fluid method (VOF) [3–6], and level set method [7–9]. Recent attempts to simulate boiling with diffuse interface approaches such as diffuse interface method [10, 11], phase field method [12, 13], and Lattice Boltzmann Equation (LBE) method [14–18] offer new capabilities in dealing with complex interface morphologies and topological changes, near-critical fluid, and motion of a contact line along a solid surface [19].

LBE methods have shown great success in simulating two-phase fluid flows with its mesoscopic nature [20–23]. In order to enable liquid-vapor phase change in LBE methods, either they are equipped with the non-ideal gas equation of state (EOS) [14, 15, 17] or an interfacial source term is added to governing equations [16, 18]. While using EOS seems to offer a more straightforward path to simulate phase change problems, it exhibits difficulties in simulating systems away from the critical temperature. Adding an interfacial source term due to phase change to corresponding governing equation is promising in terms of enabling phase change problems with a large liquid-to-vapor density ratio and a better control over mass flux at the interface. In almost all recent numerical works on modeling liquid-vapor

phase change using LBE methods [16, 18], the interfacial source term is spread over a diffuse phase interface offering little control over the phase interface temperature. The sharp interface treatment of the interfacial source term by macroscopic internal energy equation provides a more accurate estimation of the mass flux at the phase interface and a better control over the phase interface temperature.

Furthermore, the benchmark problems with available theoretical solutions utilized for validation of phase change models in most recent studies include single-phase Stefan problems with different thermal configurations [3, 5, 18]. Although validation of these benchmarks proves some capabilities of the phase change models, by using more relevant benchmarks such as two-phase Stefan and two-phase sucking interface problems, the validations become more comprehensive, which provide situations close to a real boiling. In both two-phase Stefan and sucking interface problems, all liquid and vapor pertinent thermophysical properties are employed in the theoretical solution [24].

In this study, the original two-phase LBE method of He *et al.* [20] (as an Eulerian-based approach for phase interface tracking) modified by Lee and Lin [25] and also equipped with the a potential form of surface tension [26] to eliminate the parasitic currents, is extended to model liquid-vapor phase change heat transfer. This modification is denoted as a *pressure-based approach*, in which an interfacial mass flow rate is added as a source term in the pressure evolution equation. The temperature distribution in the system is obtained by solving the sharp interface macroscopic energy equation discretized with an isotropic finite difference scheme. This paper is organized as follows. Section II describes the phase change model and the LBE method. In section III, the proposed phase change model is verified against theoretical solutions of two-phase Stefan and two-phase sucking interface problems, and a liquid droplet evaporation in a superheated vapor, a vapor bubble growth in a superheated liquid, and a vapor bubble rising in a superheated liquid are studied in detail. The concluding remarks are reported in section IV.

II. PHYSICAL MODEL AND NUMERICAL ALGORITHM

In this section, the phase change model, and the discrete and lattice Boltzmann equations are presented.

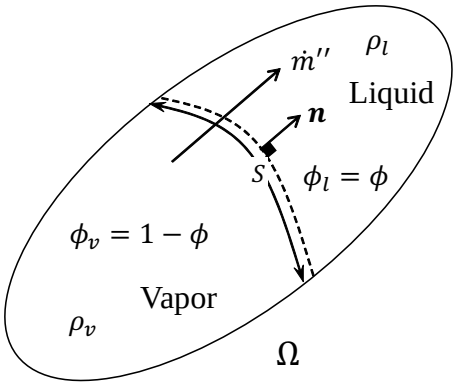

FIG. 1: A schematic of a liquid-vapor system with the phase interface.

A. Liquid-Vapor Phase Change Model

Consider a volume element Ω containing a part of the phase interface with the surface area of S between liquid and vapor in Fig. 1. The unit normal vector to the phase interface, mass flux, local density, liquid bulk density, and vapor bulk density are denoted by $\mathbf{n} = \frac{\nabla\rho}{|\nabla\rho|}$, $\dot{m}''$, ρ, ρ_l, and ρ_v, respectively. The volume fraction, $\phi = (\rho - \rho_v)/(\rho_l - \rho_v)$, is based on liquid phase, therefore $\phi_l = \phi$ and $\phi_v = 1 - \phi$ $(0 \leq \phi \leq 1)$ where the subscripts l, and v refer to liquid and vapor, respectively. For fluid flows with phase change, the same approach in [27] is utilized for the continuity equation in each phase except an extra source term $(\pm\dot{m}''')$ corresponding to the mass flow rate per unit volume is added for each phase [4, 18]. The continuity equation can be derived by combining the continuity equations for liquid and vapor phases,

$$\nabla \cdot \mathbf{u} = \dot{m}''' \left(\frac{1}{\rho_v} - \frac{1}{\rho_l} \right), \tag{1}$$

where $\mathbf{u}$ is the macroscopic velocity. The divergence of velocity in Eq. (1) is zero everywhere except for nodes around the phase interface called *Interface Neighboring* (INB) nodes, as shown in Fig. 2. The divergence of velocity at the phase interface corresponds to volume change due to phase change, which is positive in the case of evaporation and negative in the case of condensation by convention. The same convention applies to the interfacial mass flux. By forcing the divergence of velocity described in Eq. (1), the energy balance at the phase interface is satisfied automatically and it causes the phase interface to move based on the sign of the mass flux.

The corresponding pressure evolution equation that is to be recovered by the lattice Boltzmann equation (LBE) described in the next section is derived from the continuity

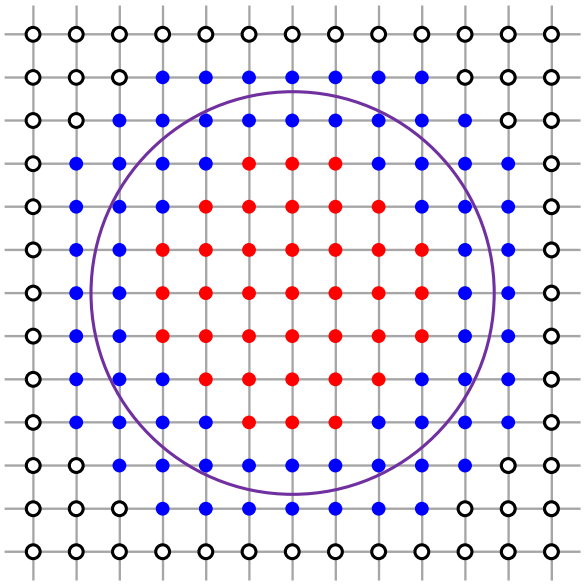

FIG. 2: INB nodes (solid blue circles) surrounding the phase interface (open circles: vapor bulk nodes, solid red circles: liquid bulk nodes).

equation,

$$\frac{\partial p}{\partial t} + \rho \frac{\partial p}{\partial \rho} \nabla \cdot \mathbf{u} + \mathbf{u} \cdot \nabla p = \rho c_s^2 \left[\dot{m}''' \left(\frac{1}{\rho_v} - \frac{1}{\rho_l} \right) \right], \tag{2}$$

where p is the pressure, t is time, and $\partial_\rho p = c_s^2 = 1/3$ is the square of lattice speed of sound. In the low frequency limit, $\partial_t p$ and $\mathbf{u} \cdot \nabla p$ become on the order of the truncation error and can be ignored recovering Eq. (1) [28]. Therefore, we can force continuity equation presented in Eq. (1) in the system by recovering the pressure evolution equation in the LBE framework. Now we can substitute Eq. (2) into the governing LBE for boiling two-phase flows.

B. Discrete Boltzmann Equations

The tracking of the density of a single-component two-phase fluid is given by the following discrete Boltzmann equation (DBE) [29–31]:

$$\frac{D f_\alpha}{D t} = -\frac{1}{\lambda}(f_\alpha - f_\alpha^{eq}) + \frac{(\mathbf{e}_\alpha - \mathbf{u}) \cdot \mathbf{F}}{c_s^2} \Gamma_\alpha(\mathbf{u}), \tag{3}$$

where α, f_α, f_α^{eq}, $\mathbf{e}_\alpha$, λ, and $\mathbf{F}$ are the characteristic direction, discrete particle density distribution function, discrete equilibrium particle density distribution function, particle microscopic velocity in the α-direction, relaxation parameter, and the forcing term, respectively

and $\Gamma_\alpha(\mathbf{u})$=$f_\alpha^{eq}/\rho$. The material derivative can be expanded as $D/Dt = \left(\frac{\partial}{\partial t} + \mathbf{e}_\alpha \cdot \nabla\right)$. The Maxwell-Boltzmann distribution of f_α^{eq} is expanded up to second order in terms of macroscopic velocity $O(\mathbf{u}^2)$:

$$f_\alpha^{eq} = t_\alpha \rho \left[1 + \frac{(\mathbf{e}_\alpha \cdot \mathbf{u})}{c_s^2} + \frac{(\mathbf{e}_\alpha \cdot \mathbf{u})^2}{2c_s^4} - \frac{(\mathbf{u} \cdot \mathbf{u})}{2c_s^2}\right], \tag{4}$$

where t_α is the weight in the α-direction [32]. The D2Q9 and D3Q27 lattices are implemented in this study for two- and three-dimensional problems, respectively. The particle microscopic velocity in the corresponding α-direction for D2Q9 square lattice is extended from D1Q3 lattice as [29],

$$\mathbf{e}_\alpha = \begin{cases} (0,0) & \alpha = 0, \\ (\cos\Theta_\alpha, \sin\Theta_\alpha) & \alpha = 1,3,5,7, \\ \sqrt{2}(\cos\Theta_\alpha, \sin\Theta_\alpha) & \alpha = 2,4,6,8, \end{cases} \tag{5}$$

where $\Theta_\alpha = (\alpha - 1)\pi/4$ and with the weights $t_0 = 4/9$, $t_1 = t_3 = t_5 = t_7 = 1/9$, and $t_2 = t_4 = t_6 = t_8 = 1/36$ [29]. The microscopic velocity and weight in D3Q27 lattice are extended from D1Q3 method as well.

The following form for the forcing term $\mathbf{F}$ can be derived by considering the mean-field approximation and excluding the volume of molecules [26]:

$$\mathbf{F} = \nabla \rho c_s^2 - \nabla p - \rho \nabla \mu + \rho \mathbf{g}, \tag{6}$$

where $\mathbf{g}$ is the gravitational acceleration. The non-classical form of the chemical potential $\mu = \partial_\rho E_0 - \kappa \nabla^2 \rho$ is placed in the third term of Eq. (6), which accounts for the separation of phases and results in a volumetric surface tension force. The bulk energy is given by $E_0(\rho) = \beta(\rho - \rho_l)^2(\rho - \rho_v)^2$ with κ and β being the gradient parameter and the bulk energy constant, respectively. In a one-dimensional plane interface at equilibrium, the density profile across the phase interface can be given by:

$$\rho(z) = \frac{\rho_l + \rho_v}{2} + \frac{\rho_l - \rho_v}{2} \tanh\left(\frac{2z}{D}\right), \tag{7}$$

where z is the normal distance from the phase interface and $D = \frac{4}{(\rho_l - \rho_v)}\sqrt{\frac{\kappa}{2\beta}}$ is the phase interface thickness. The surface tension can be chosen as a numerical parameter and given by $\sigma = \frac{(\rho_l - \rho_v)}{6}\sqrt{2\kappa\beta}$ [33].

Eq. (3) recovers the continuity equation

$$\frac{\partial \rho}{\partial t} + \nabla \cdot (\rho \mathbf{u}) = 0. \tag{8}$$

A second distribution function is introduced by the transform, $g_\alpha = c_s^2 f_\alpha + (p - \rho c_s^2)\,\Gamma_\alpha(0)$, for pressure and momentum in the system as in [25]. When substituted into Eq. (3), its material derivative becomes:

$$\frac{Dg_\alpha}{Dt} = c_s^2 \frac{Df_\alpha}{Dt} + \left(\frac{Dp}{Dt} - c_s^2 \frac{D\rho}{Dt}\right)\Gamma_\alpha(0). \tag{9}$$

The last two terms inside the parentheses on the right-hand side of Eq. (9) can be recast due to the pressure evolution equation Eq. (2) and the continuity equation Eq. (8), respectively:

$$\frac{Dp}{Dt} = (\mathbf{e}_\alpha - \mathbf{u}) \cdot \nabla p - \rho c_s^2 \nabla \cdot \mathbf{u} + \rho c_s^2 \left[\dot{m}''' \left(\frac{1}{\rho_v} - \frac{1}{\rho_l}\right)\right], \tag{10}$$

and

$$c_s^2 \frac{D\rho}{Dt} = (\mathbf{e}_\alpha - \mathbf{u}) \cdot \nabla \rho c_s^2 - \rho c_s^2 \nabla \cdot \mathbf{u}. \tag{11}$$

Substituting Eqs. (10) and (11) into Eq. (9) forms the following discrete Boltzmann equation for pressure and momentum:

$$\begin{aligned}\frac{Dg_\alpha}{Dt} = &-\frac{1}{\lambda}(g_\alpha - g_\alpha^{eq}) + (\mathbf{e}_\alpha - \mathbf{u}) \cdot \left[\nabla \rho c_s^2 (\Gamma_\alpha(\mathbf{u}) - \Gamma_\alpha(0)) - \rho \nabla \mu \Gamma_\alpha(\mathbf{u})\right] \\ &+ \rho c_s^2 \left[\dot{m}''' \left(\frac{1}{\rho_v} - \frac{1}{\rho_l}\right)\right] \Gamma_\alpha(0),\end{aligned} \tag{12}$$

in which $(\mathbf{e}_\alpha - \mathbf{u}) \cdot \nabla p (\Gamma_\alpha(\mathbf{u}) - \Gamma_\alpha(0)) \sim O(Ma^3)$ is dropped due to the low Mach number approximation [25]. For simplicity, the gravity term in Eq. (12) and from now on is omitted. The last term on the right-hand side of Eq. (12) activates phase change in the system.

The macroscopic equations recovered by first and second order Chapman-Enskog expansion of Eq. (12) are the pressure evolution and the momentum equations for non-ideal gases, respectively:

$$\frac{\partial p}{\partial t} + \rho c_s^2 \nabla \cdot \mathbf{u} = \rho c_s^2 \left[\dot{m}''' \left(\frac{1}{\rho_v} - \frac{1}{\rho_l}\right)\right], \tag{13}$$

and

$$\frac{\partial (\rho \mathbf{u})}{\partial t} + \nabla \cdot (\rho \mathbf{u}\mathbf{u}) = -\nabla p - \rho \nabla \mu + \nabla \cdot \left[\eta (\nabla \mathbf{u} + \nabla^T \mathbf{u})\right], \tag{14}$$

with η being the dynamic viscosity.

C. Calculation of Interfacial Mass Flux, $\dot{m}''$, and Mass Flow Rate, $\dot{m}'''$

In order to find a correct formulation for the mass flow rate at phase interface $\dot{m}'''$, the interfacial mass flux $\dot{m}''$ is considered. The mass flux can be obtained by two different sharp

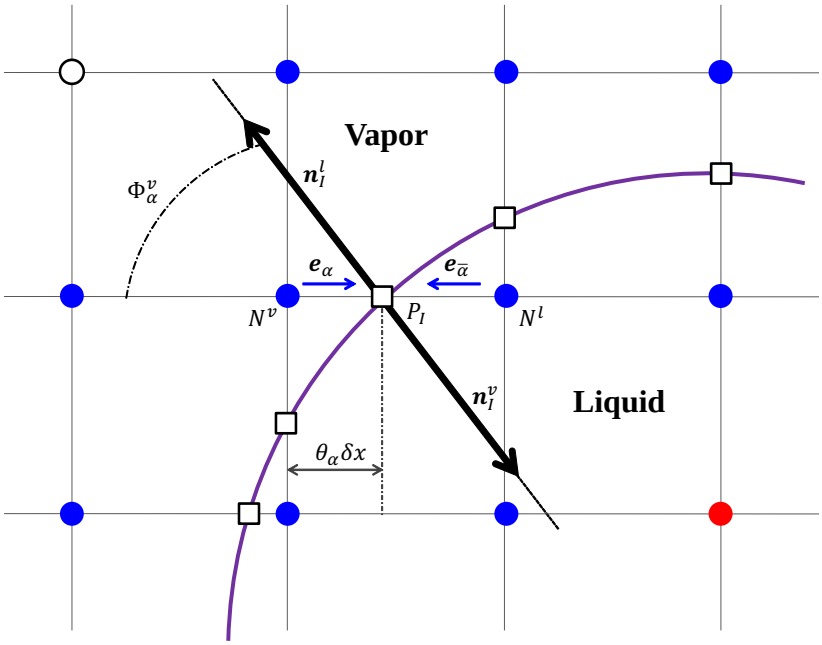

FIG. 3: Illustration of a phase interface curve in the regular lattice structure with normal vectors to phase interface (solid blue circles: INB nodes, open circles: vapor bulk nodes, solid red circles: liquid bulk nodes, open squares: phase interface points. See text for notations and definitions.).

interface approaches. First approach considers the momentum balance across the phase interface [9],

$$\dot{m}'' = \rho_v \left(\mathbf{u}_v - \mathbf{u}_I\right) \cdot \mathbf{n} = \rho_l \left(\mathbf{u}_l - \mathbf{u}_I\right) \cdot \mathbf{n}, \tag{15}$$

where $\mathbf{u}_l$, $\mathbf{u}_v$, and $\mathbf{u}_I$ are liquid, vapor, and phase interface velocities, respectively. In the second approach, the mass flux is related to the heat flux difference across the phase interface by using the energy balance at the phase interface [9],

$$\dot{m}'' h_{fg} = q_v - q_l, \tag{16}$$

where term h_{fg} refers to the latent heat of vaporization or heat of evaporation. q_v and q_l represent the normal heat fluxes at phase interface point in vapor-side and liquid-side of the phase interface, respectively. Eq. (16) is called Rankine-Hugoniot jump condition [9]. In the present work, the second approach is implemented to find the mass flux, since the numerical treatment of Eq. (15) is not preferred **because the phase interface velocity in Eq. (15) in not available unless the interfacial mass flux is added to the system. Using Eq. (16) enables us to use heat flux from temperature distribution in each side**

of the phase interface and to calculate interfacial mass flux accurately without a need to recall the phase interface velocity. After finding the interfacial mass flux and adding it to the system, the phase interface moves in the correct direction and its velocity can be extracted as well.

The sharp interface treatment of interfacial mass flux lays down its calculation only on the phase interface location which may not coincide with lattice nodes. The nodes surrounding the phase interface are referred as INB nodes. The INB nodes located in both liquid and vapor phases are filtered out using the following criterion,

$$\exists \alpha \neq 0 \quad s.t. \quad [\phi(\mathbf{x},t) - \phi_I] \times [\phi(\mathbf{x} + \mathbf{e}_\alpha \delta t, t) - \phi_I] < 0, \tag{17}$$

where $\phi_I = 0.5$ is the volume fraction at the phase interface and δt is the time step in LBE framework which is set to 1. In Fig. 2, the INB nodes are shown with solid blue circles and they all satisfy the condition in Eq. (17). As shown in Fig. 3, consider two INB nodes on the vapor-side (N^v) and in the liquid-side (N^l) of the phase interface connected by $\mathbf{e}_\alpha$ characteristic direction. The phase interface point between these two nodes is shown by P_I and is located in Cartesian coordinates $\mathbf{x}_{P_I} = (x_I, y_I)$. The phase interface point can be described as the location where the phase interface curve crosses the characteristic direction $\mathbf{e}_\alpha$ starting from N^v. Phase interface points in the diagonal characteristic directions are omitted in Fig. 3 for the sake of simplicity. At the phase interface point P_I, the liquid outward unit normal vector is depicted as $\mathbf{n}_I^l$ and the vapor one has the same magnitude but with a different sign, ($\mathbf{n}_I^v = -\mathbf{n}_I^l$). The goal is to find the sharp interface heat flux jump at P_I along the normal direction $\mathbf{n}_I^v$ (or $\mathbf{n}_I^l$) and then map it along the $\mathbf{e}_\alpha$ direction since the points crossing the lattice structure in the normal direction $\mathbf{n}_I^v$ or $\mathbf{n}_I^l$ are not necessarily coincide with lattice nodes.

The heat fluxes at phase interface point P_I in vapor- and liquid-side of the phase interface can be written as,

$$q_v = -k_v \mathbf{n}_I^v \cdot \nabla T_I^v, \tag{18}$$

$$q_l = -k_l \mathbf{n}_I^l \cdot \nabla T_I^l, \tag{19}$$

where ∇T_I^v and ∇T_I^l are the temperature gradients on the vapor-side and liquid-side of the phase interface, respectively. The parameters k_v and k_l are the thermal conductivities. A constant saturation temperature, T_{sat}, is assumed in the calculation of heat fluxes at phase

interface point P_I. It should be noted that the sharp interface treatment of the heat fluxes ensures accurate calculation of the mass flux due to phase change and easy control of the phase interface temperature.

Using the characteristic direction $\mathbf{e}_\alpha$, the normal temperature gradient on the vapor-side at phase interface point P_I can be recast as [34],

$$\mathbf{n}_I^v \cdot \nabla T_I^v = \frac{\mathbf{e}_\alpha \cdot \nabla T_I^v}{\mathbf{n}_I^v \cdot \mathbf{e}_\alpha}. \tag{20}$$

The proof of Eq. (20) is provided in Appendix A. Eq. (20) uses the directional gradient of temperature in $\mathbf{e}_\alpha$ direction to approximate the normal temperature gradient in $\mathbf{n}_I^v$ direction. Similar relation can be used for the normal temperature gradient in the liquid-side of the phase interface. Therefore, the heat fluxes normal to the phase interface at P_I in the vapor- and liquid-side of the phase interface are,

$$q_v = -k_v \frac{\mathbf{e}_\alpha \cdot \nabla T_I^v}{\mathbf{n}_I^v \cdot \mathbf{e}_\alpha}, \tag{21}$$

$$q_l = -k_l \frac{\mathbf{e}_{\bar{\alpha}} \cdot \nabla T_I^l}{\mathbf{n}_I^l \cdot \mathbf{e}_{\bar{\alpha}}}, \tag{22}$$

where $\mathbf{e}_{\bar{\alpha}} = -\mathbf{e}_\alpha$. The normal vectors $\mathbf{n}_I^v$ and $\mathbf{n}_I^l$ at P_I are not available since they do not reside on the lattice nodes.

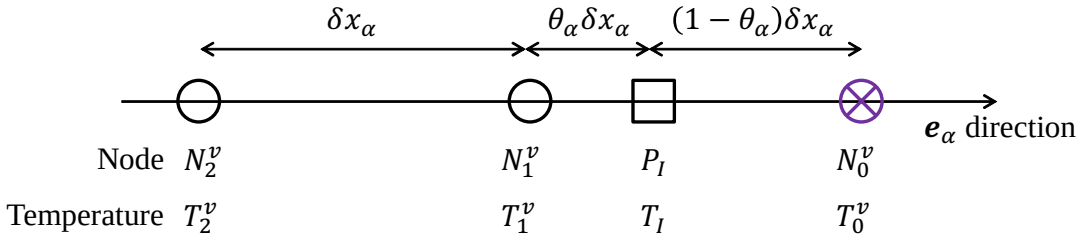

FIG. 4: Temperature gradient calculation at phase interface point P_I on the vapor-side using the temperatures of the phase interface (T_I), the neighboring lattice nodes (T_1^v and T_2^v) in the vapor phase, and the ghost node (T_0^v).

In order to calculate the temperature gradient at the phase interface point P_I on the vapor-side as shown in Eq. (21), consider the phase interface point P_I, two lattice nodes on the vapor-side of the phase interface N_1^v and N_2^v, and a ghost node N_0^v in Fig. 4 where $\delta x_\alpha = |\mathbf{e}_\alpha|\, \delta t$ is the spatial step in the characteristic direction α. Ghost nodes are considered

in the opposite side of each phase to facilitate the temperature gradient calculation. The temperature at the ghost node T_0^v is calculated in $\mathbf{e}_\alpha$ direction as in [35] to avoid singularity,

$$T_0^v = \frac{2T_I + (\theta_\alpha - 1)T_2^v}{1 + \theta_\alpha}, \tag{23}$$

where T_I is the phase interface temperature set to a constant saturation temperature T_{sat} in this study, θ_α is the normalized distance between P_I and the first lattice node N_1^v in $\mathbf{e}_\alpha$ direction, and T_2^v is the temperature at the second lattice node N_2^v. By having the definition of temperature at the ghost node T_0^v, the temperature gradient at P_I on the vapor-side is calculated with the following second-order formula [36],

$$\mathbf{e}_\alpha \cdot \nabla T_I^v = \frac{(1 + 2\theta_\alpha)T_0^v - 4\theta_\alpha T_1^v - (1 - 2\theta_\alpha)T_2^v}{2\delta t}. \tag{24}$$

Since the temperature gradient in Eq. (21) is calculated using the sharp interface approach, only the temperature of lattice nodes T_1^v and T_2^v on the vapor-side and the temperature of the ghost node T_0^v are considered in Eq. (24). Likewise, the same treatment is applied for temperature gradient at P_I in liquid-side of the phase interface.

The normal heat flux jump, $\langle q \rangle$, at P_I is then written as,

$$\langle q \rangle = q_v - q_l = -k_v \frac{\mathbf{e}_\alpha \cdot \nabla T_I^v}{\mathbf{n}_I^v \cdot \mathbf{e}_\alpha} + k_l \frac{\mathbf{e}_{\bar{\alpha}} \cdot \nabla T_I^l}{\mathbf{n}_I^l \cdot \mathbf{e}_{\bar{\alpha}}}. \tag{25}$$

Substituting Eq. (25) into Eq. (16) yields the following equation for the interfacial mass flux due to phase change at P_I,

$$\dot{m}'' = \frac{1}{h_{fg}} \left[-k_v \frac{\mathbf{e}_\alpha \cdot \nabla T_I^v}{\mathbf{n}_I^v \cdot \mathbf{e}_\alpha} + k_l \frac{\mathbf{e}_{\bar{\alpha}} \cdot \nabla T_I^l}{\mathbf{n}_I^l \cdot \mathbf{e}_{\bar{\alpha}}} \right]. \tag{26}$$

The mass flux at P_I can be distributed on neighboring nodes along either $\mathbf{n}_I^v$ or $\mathbf{n}_I^l$, but these vectors do not generally pass through lattice nodes. Alternatively, we find the component of mass flux in a given characteristic direction $\mathbf{e}_\alpha$.

As shown in Fig. 3, the angle formed by the characteristic direction $\mathbf{e}_\alpha$ and the normal vector $\mathbf{n}_I^v$ at the phase interface point is Φ_α^v and is calculated by the inner product of the two vectors,

$$\cos(\Phi_\alpha^v) = \frac{\mathbf{n}_I^v \cdot \mathbf{e}_\alpha}{|\mathbf{n}_I^v| \, |\mathbf{e}_\alpha|}. \tag{27}$$

The interfacial mass flux at P_I can be mapped in $\mathbf{e}_\alpha$ direction using the angle Φ_α^v,

$$\dot{m}''_{\mathbf{e}_\alpha} = \dot{m}'' \cos(\Phi_\alpha^v). \tag{28}$$

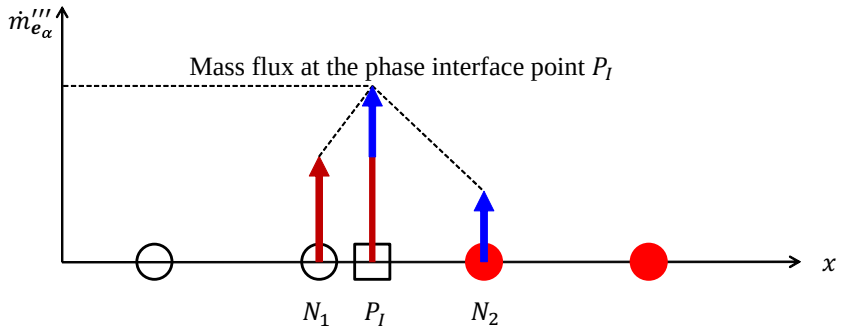

FIG. 5: The mass flux at the phase interface point P_I distributed by a linear weighting function on lattice nodes.

With this definition, the component of the mass flux in $\mathbf{e}_\alpha$ direction in Eq. (28) is expressed by,

$$\dot{m}''_{\mathbf{e}_\alpha} = \dot{m}'' \frac{\mathbf{n}_I^v \cdot \mathbf{e}_\alpha}{|\mathbf{n}_I^v|\,|\mathbf{e}_\alpha|}. \tag{29}$$

Finally, Eq. (26) is substituted for the mass flux in Eq. (29),

$$\dot{m}''_{\mathbf{e}_\alpha} = \frac{1}{h_{fg}} \frac{\mathbf{n}_I^v \cdot \mathbf{e}_\alpha}{|\mathbf{n}_I^v|\,|\mathbf{e}_\alpha|} \left[-k_v \frac{\mathbf{e}_\alpha \cdot \nabla T_I^v}{\mathbf{n}_I^v \cdot \mathbf{e}_\alpha} + k_l \frac{\mathbf{e}_{\bar{\alpha}} \cdot \nabla T_I^l}{\mathbf{n}_I^l \cdot \mathbf{e}_{\bar{\alpha}}} \right], \tag{30}$$

which can then be further simplified as follows,

$$\dot{m}''_{\mathbf{e}_\alpha} = \frac{1}{h_{fg}\,|\mathbf{e}_\alpha|} \left(-k_v \mathbf{e}_\alpha \cdot \nabla T_I^v + k_l \mathbf{e}_{\bar{\alpha}} \cdot \nabla T_I^l \right), \tag{31}$$

due to $|\mathbf{n}_I^v| = 1$.

The mass flux component $\dot{m}''_{\mathbf{e}_\alpha}$ needs to be converted to volumetric mass flow rate $\dot{m}'''$ to be used in Eq. (1) and subsequent equations. Consider a mass flux $\dot{m}''_{\mathbf{e}_\alpha}$ at P_I as shown in Fig. 5. It is then distributed to neighboring lattice nodes (N_1 and N_2) using a linear weighting function [37],

$$\dot{m}'''_{\mathbf{e}_\alpha}(\mathbf{x}) = \frac{1}{\delta x} \dot{m}''_{\mathbf{e}_\alpha} \Psi'(r), \tag{32}$$

where $\dot{m}'''_{\mathbf{e}_\alpha}$ is the mass flow rate at neighboring lattice nodes around P_I and the Ψ' is the linear weighting function defined as,

$$\Psi'(r) = \begin{cases} 1 - r, & \text{if } r \le 1 \\ 0. & \text{if } r \ge 1 \end{cases}, \tag{33}$$

where the non-dimensional argument is set to $r = |\mathbf{x} - \mathbf{x}_{P_I}| / |\mathbf{e}_\alpha|\,\delta t$.

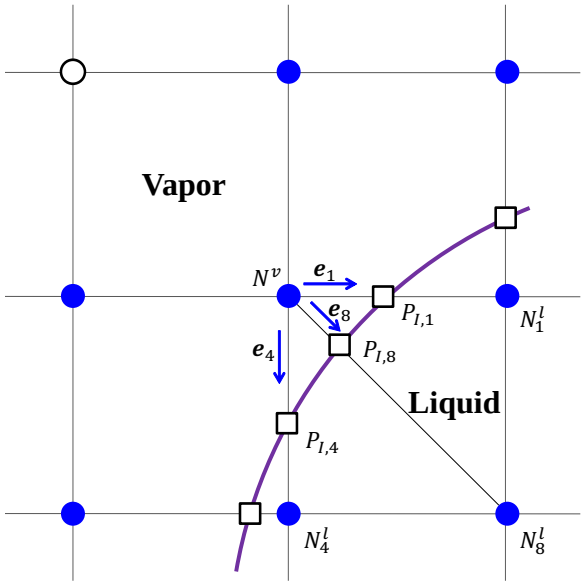

FIG. 6: Illustration of different phase interface points on different characteristic directions starting from point N^v in the vapor phase.

To summarize, the mass flux is first calculated at the phase interface location P_I on a link between a pair of lattice nodes, one in vapor side and the other in liquid side in $\mathbf{e}_\alpha$ direction as depicted in Fig. 5. The mass flux is then distributed on the adjacent lattice nodes (*e.g.* N_1 and N_2) in the $\mathbf{e}_\alpha$ direction. The distributed mass flux is called the mass flow rate.

The application of the linear weighting function not only distributes the mass flux at phase interface point but also it finds the link between the sharp interface mass flux and the mass flow rate at phase interface between liquid and vapor. Another way to distribute the mass flux at the phase interface point P_I is to multiply it by the absolute value of the gradient of the volume fraction $|\nabla\phi|$ [18]. However, using $|\nabla\phi|$ does not guarantee the same initial diffusive profile as the phase interface undergoes deformation during the simulation runtime.

The INB nodes may cross the phase interface curve in multiple $\mathbf{e}_\alpha$ directions. Consequently, different mass flow rates $\dot{m}'''_{\mathbf{e}_\alpha}$ may be found at one lattice node in each $\mathbf{e}_\alpha$ direction. A weighted averaging process is needed in this situation. Here we choose $\dot{m}'''_{\mathbf{e}_\alpha}$ in the dominant characteristic direction, which is defined as the direction of maximum inner product $(\mathbf{e}_\alpha \cdot \mathbf{n}_I^v)/|\mathbf{e}_\alpha|$ or $(\mathbf{e}_\alpha \cdot \mathbf{n}_I^l)/|\mathbf{e}_\alpha|$ at P^v. As an example in D2Q9 lattice structure, the lattice node N^v crosses the phase interface curve at $P_{I,1}$, $P_{I,4}$, and $P_{I,8}$ in $\mathbf{e}_1$, $\mathbf{e}_4$, and $\mathbf{e}_8$ characteristic directions, respectively as shown in Fig. 6. Three different mass flow rates are then

obtained as $\dot{m}'''_{\mathbf{e}_1}$, $\dot{m}'''_{\mathbf{e}_4}$, and $\dot{m}'''_{\mathbf{e}_8}$ at lattice node N^v, and $\dot{m}'''_{\mathbf{e}_8}$ is finally chosen as $\dot{m}'''_{\mathbf{e}_\alpha}$ in Eq. (1).

D. Macroscopic Internal Energy Equation

The sharp interface macroscopic energy equation is considered for solving the temporal and spatial evolution of the temperature in the vapor and liquid phases:

$$\frac{\partial T}{\partial t} + \mathbf{u} \cdot \nabla T = \chi \nabla^2 T, \tag{34}$$

where the χ, T, and $\mathbf{u}$ are the thermal diffusivity, temperature, and local velocity, respectively. Due to the sharp interface energy solver, the thermal diffusivity in the vapor phase becomes χ_v and in the liquid phase becomes χ_l. The energy jump condition due to phase change that includes the latent heat h_{fg} and mass flow rate $\dot{m}'''$ is embedded in the definition of divergence of velocity in Eq. (1). Therefore the local velocity in Eq. (34) carries information related to latent heat and mass flow rate at the interface and its profiles shows a jump at the phase interface due to the phase change at the phase interface.

The macroscopic energy equation is then discretized with the explicit Euler method in time and the 2nd-order accurate isotropic finite difference method [25] in space:

$$\begin{aligned} \nabla T &= \textstyle\sum_{\alpha\neq 0} \frac{t_\alpha \mathbf{e}_\alpha [T(\mathbf{x}+\mathbf{e}_\alpha \delta t) - T(\mathbf{x}-\mathbf{e}_\alpha \delta t)]}{2c_s^2 \delta t}, \\ \nabla^2 T &= \textstyle\sum_{\alpha\neq 0} \frac{t_\alpha [T(\mathbf{x}+\mathbf{e}_\alpha \delta t) - 2T(\mathbf{x}) + T(\mathbf{x}-\mathbf{e}_\alpha \delta t)]}{c_s^2 \delta t^2}. \end{aligned} \tag{35}$$

In Eq. (35) on lattice nodes near the phase interface, the $T(\mathbf{x} + \mathbf{e}_\alpha \delta t)$ or $T(\mathbf{x} - \mathbf{e}_\alpha \delta t)$ may point to the temperature in the other phase and thus require the ghost nodes defined for calculation of the heat flux in Eq. (24) as well.

E. Lattice Boltzmann Equations

The discrete Boltzmann equations for the density in Eq. (3) and the pressure and momentum in Eq. (12) are discretized along the characteristics over time step δt as in [25]. By defining the following modified discrete distribution functions,

$$\bar{f}_\alpha = f_\alpha + \frac{f_\alpha - f_\alpha^{eq}}{2\tau} - \frac{\delta t}{2} \frac{(\mathbf{e}_\alpha - \mathbf{u}) \cdot [\nabla \rho c_s^2 - \nabla p - \rho \nabla \mu)]\, \Gamma_\alpha(\mathbf{u})}{c_s^2}. \tag{36}$$

and

$$\bar{g}_\alpha = g_\alpha + \frac{g_\alpha - g_\alpha^{eq}}{2\tau} - \frac{\delta t}{2}(\mathbf{e}_\alpha - \mathbf{u}) \cdot \left[\nabla \rho c_s^2 (\Gamma_\alpha(\mathbf{u}) - \Gamma_\alpha(0)) - \rho \nabla \mu \Gamma_\alpha(\mathbf{u})\right] - \frac{\delta t}{2} \rho c_s^2 \left[\dot{m}''' \left(\frac{1}{\rho_v} - \frac{1}{\rho_l}\right)\right] \Gamma_\alpha(0). \tag{37}$$

The lattice Boltzmann equations at a lattice site ($\mathbf{x}$) can be written as:

$$\bar{f}_\alpha(\mathbf{x}, t) - \bar{f}_\alpha(\mathbf{x} - \mathbf{e}_\alpha \delta t, t - \delta t) = -\frac{1}{\tau + 0.5} \left(\bar{f}_\alpha - \bar{f}_\alpha^{eq}\right)\Big|_{(\mathbf{x} - \mathbf{e}_\alpha \delta t, t - \delta t)} + \frac{\delta t (\mathbf{e}_\alpha - \mathbf{u}) \cdot \left[\nabla \rho c_s^2 - \nabla p - \rho \nabla \mu\right] \Gamma_\alpha(\mathbf{u})}{c_s^2}\Big|_{(\mathbf{x} - \mathbf{e}_\alpha \delta t, t - \delta t)}, \tag{38}$$

and

$$\bar{g}_\alpha(\mathbf{x}, t) - \bar{g}_\alpha(\mathbf{x} - \mathbf{e}_\alpha \delta t, t - \delta t) = -\frac{1}{\tau + 0.5} \left(\bar{g}_\alpha - \bar{g}_\alpha^{eq}\right)\Big|_{(\mathbf{x} - \mathbf{e}_\alpha \delta t, t - \delta t)} + \delta t (\mathbf{e}_\alpha - \mathbf{u}) \cdot \left[\nabla \rho c_s^2 (\Gamma_\alpha(\mathbf{u}) - \Gamma_\alpha(0)) - \rho \nabla \mu \Gamma_\alpha(\mathbf{u})\right]\Big|_{(\mathbf{x} - \mathbf{e}_\alpha \delta t, t - \delta t)} + \delta t \rho c_s^2 \left[\dot{m}''' \left(\frac{1}{\rho_v} - \frac{1}{\rho_l}\right)\right] \Gamma_\alpha(0)\Big|_{(\mathbf{x} - \mathbf{e}_\alpha \delta t, t - \delta t)}, \tag{39}$$

where $\tau = \lambda / \delta t$ is the non-dimensional relaxation parameter.

The macroscopic variables such as density, momentum, and pressure can be calculated by taking the moments of modified distribution functions $\bar{f}_\alpha$ and $\bar{g}_\alpha$:

$$\rho = \sum_\alpha \bar{f}_\alpha, \tag{40}$$

$$\rho \mathbf{u} = \frac{1}{c_s^2} \sum_\alpha \mathbf{e}_\alpha \bar{g}_\alpha - \frac{\delta t}{2} \rho \nabla \mu, \tag{41}$$

$$p = \sum_\alpha \bar{g}_\alpha + \frac{\delta t}{2} \mathbf{u} \cdot \nabla \rho c_s^2 + \frac{\delta t}{2} \rho c_s^2 \left[\dot{m}''' \left(\frac{1}{\rho_v} - \frac{1}{\rho_l}\right)\right]. \tag{42}$$

Viscosity and relaxation parameter are constant in each bulk phase but vary in the interfacial region. The relaxation parameter is inversely proportional to the volume fraction:

$$\frac{1}{\tau} = \frac{1}{\tau_v} + \left(\frac{1}{\tau_l} - \frac{1}{\tau_v}\right) \phi(\mathbf{x}, t). \tag{43}$$

where the parameters τ_l and τ_v are relaxation parameters for liquid and vapor phases, respectively. The heat conductivity k, specific heat c_p, and thermal diffusivity χ are constant in each bulk phase and have a jump across the phase interface.

$$k = \frac{1}{2}(k_v + k_l) + \frac{1}{2}(k_v - k_l) \operatorname{sign}[\phi_i - \phi(\mathbf{x}, t)], \tag{44}$$

$$c_p = \frac{1}{2}\left(c_{p_v} + c_{p_l}\right) + \frac{1}{2}\left(c_{p_v} - c_{p_l}\right)\mathrm{sign}[\phi_i - \phi(\mathbf{x}, t)], \tag{45}$$

$$\chi = \frac{1}{2}\left(\chi_v + \chi_l\right) + \frac{1}{2}\left(\chi_v - \chi_l\right)\mathrm{sign}[\phi_i - \phi(\mathbf{x}, t)]. \tag{46}$$

The sign function in Eq. (46), $\mathrm{sign}[\phi_i - \phi(\mathbf{x}, t)]$, yields $+1$ in the vapor phase and -1 in the liquid phase. The energy equation solver considers a sharp interface with a specified phase interface temperature and the thermal properties are not smoothed across the phase interface, instead they have a jump. This approach safeguards the accurate calculation of the interfacial mass flux which results in the correct movement of the phase interface due to liquid-vapor phase change.

The proposed LBE model for liquid-vapor phase change is different from the one introduced by Safari *et al.* [18] in many aspects as described in the following. First, the current LBE model is based on the single-component two-phase fluid flow approach and the order parameter is density while in [18], the model is based on the two-component two-phase fluid flow approach and the order parameter is composition. Second, the non-zero divergence of velocity in Eq. (1) is forced in the system by the pressure evolution equation, Eq. (13), in our model while it is added as a volumetric source term to the continuity equation in [18]. Third, the present energy equation is solved using the sharp interface while it is solved using the diffuse interface in [18]. The sharp interface treatment not only is crucial in calculating the interfacial mass flux accurately but also gives us a better control over the phase interface temperature. Accurate calculation of the mass flux is important in the small-scale boiling. In [18], since the thermal properties such as thermal conductivity and specific heat are smoothed over the interfacial region, it can not provide exact calculation of the heat flux and the mass flux. Accordingly, these properties are considered constant in each phase and exhibit a jump at phase interface in our model. Besides, in [18], the phase interface thickness is dependent on density ratios (3, 4, and 5 in lattice units for the density ratios of 10, 100, and 1000, respectively) leading to introduction of an additional free parameter in the system. The phase interface thickness is constant for all simulation cases in the current study, regardless of density ratio.

III. NUMERICAL VALIDATION

In this section the current phase change model is used to simulate one-, two-, and three-dimensional liquid-vapor phase change problems. The computational domain in all cases is a regular Cartesian lattice grid and the time step δt and grid spacing δx are equal to unity in lattice units. First, the physical model is verified against available theoretical solutions, and then the two-dimensional problem of droplet evaporation in superheated vapor and the three-dimensional problem of vapor bubble growth in superheated liquid and the three-dimensional problem of vapor bubble rising in superheated liquid are studied in detail.

A. Heat Conduction in Liquid-Vapor Systems

In this section, steady and unsteady heat conduction simulations in liquid-vapor systems are validated. The main goal is to check the accuracy of the sharp interface energy solver in the lattice Boltzmann framework which plays an important role in accurate calculation of the interfacial mass flux. First, the steady state case is discussed followed by the unsteady one in section III A 2.

1. Steady State Heat Conduction

Figure. 7 illustrates the schematic of the heat conduction in a liquid-vapor system. Both phases are bounded with a constant temperature wall. Initially, the temperature is constant in each phase ($T_l = +1$ and $T_r = -1$) and has a jump across the phase interface. However, the phase interface temperature located at the midplane is kept constant at $T_I = 0.81$ during the simulation. By neglecting the convection term in the macroscopic internal energy equation, it is simplified to,

$$\frac{\partial T}{\partial t} = \chi \frac{\partial^2 T}{\partial x^2}, \tag{47}$$

where the thermal diffusivity has a discontinuity across the phase interface as in Eq. (46). The thermal diffusivity of vapor is 10 times larger than liquid ($\chi_v = 0.1$, $\chi_l = 0.01$). The heat flux is the same everywhere creating zero heat flux jump across the phase interface. The transient macroscopic equation in Eq. (47) is iterated in time until a steady state solution is reached. Consider Fig. 8a, which plots steady state temperature profile in current method

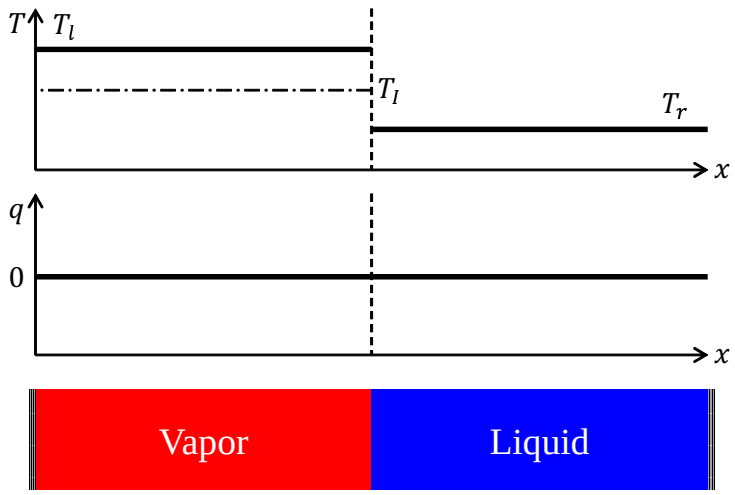

FIG. 7: A schematic of the steady state heat conduction in a liquid-vapor system along with initial temperature (T) and heat flux (q) distribution.

against the theory. There is an excellent agreement between the method and theory, and the sharp interface temperature profile at phase interface is magnified in Fig. 8b. As follows from this figure, the sharp interface internal energy solver creates a sharp transition in the temperature profile and assists in exact calculation of the heat flux jump across the phase interface.

2. Unsteady Heat Conduction

The unsteady heat conduction for the liquid-vapor system shown in Fig. 7 creates a heat flux jump at the phase interface during the simulation. The initial temperature profile in this case is slightly different from the steady state case. The left wall is kept at $T_l = 1$ and the right boundary is kept at a constant temperature of $T_r = -1$. The initial temperature of the liquid and vapor is set to the interface temperature ($T_I = 0$). Accurate calculation of transient heat flux jump at phase interface is indispensable for calculating mass flux in boiling. The goal in this section is to use a sharp interface internal energy solver to track the temperature as well as heat flux jump at phase interface and compare them with theory. The thermal diffusivities of vapor and liquid are set to 0.2 and 0.1, respectively. Figure. 9a illustrates the comparison of temperature profiles at a certain time between the current result and the theory. The same comparison for heat flux is presented in Fig. 9b. In both temperature and heat flux figures, the results match very well. As the temperature profile

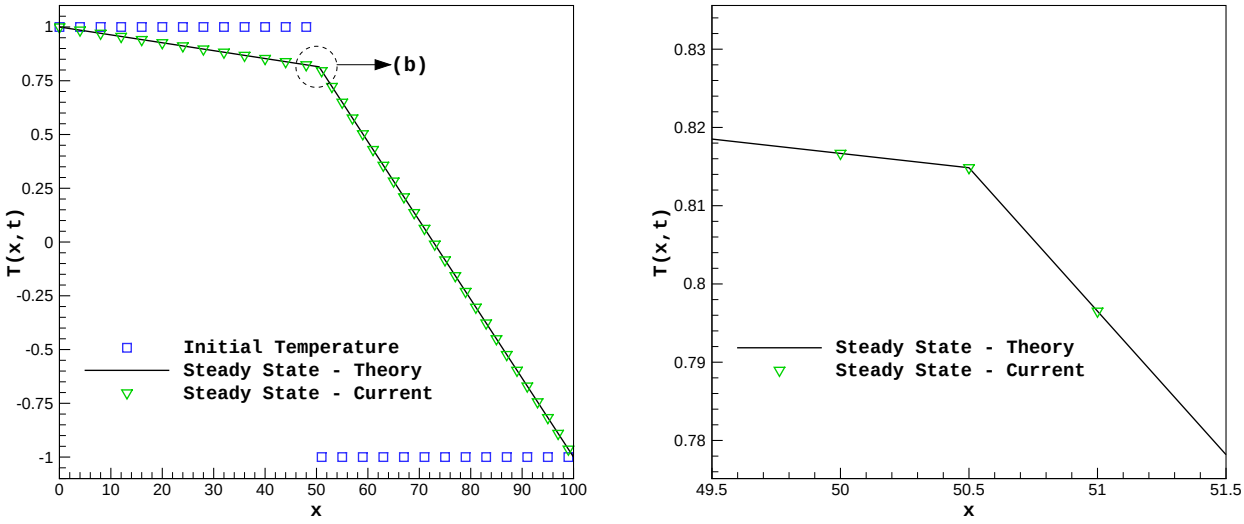

(a) (b)

FIG. 8: (a) Comparison of the temperature distribution in the steady state heat conduction problem between the current result (symbol) and the theory (line) along with initial temperature profile (square symbol) and (b) the sharp profile of the temperature across the phase interface.

evolves with time, the heat flux jump at phase interface decreases and reaches a constant value eventually. The final heat flux jump becomes $\langle q \rangle = -5.23 \times 10^{-3}$.

B. Two-Phase Stefan Problem

The classical two-phase Stefan problem construes the temperature distribution in a homogeneous medium with phase change occurring at the phase interface. An theoretical solution [24] of this problem with limited applicability can be used to validate the liquid-vapor phase transition model and to test the convergence of the current model towards the sharp interface limit. The similar benchmark for most recent studies on liquid-vapor phase change problems is the single-phase Stefan problem [3, 5] where the theoretical solution does not include the density ratio parameter and the thermophysical properties of one phase. The two-phase Stefan problem with density effect is considered a more realistic benchmark for phase change models since the theoretical solution encompasses all liquid and vapor thermophysical properties and there is no free parameter in the system.

The problem geometry and initial temperature profile is depicted in Fig. 10. In the theory,

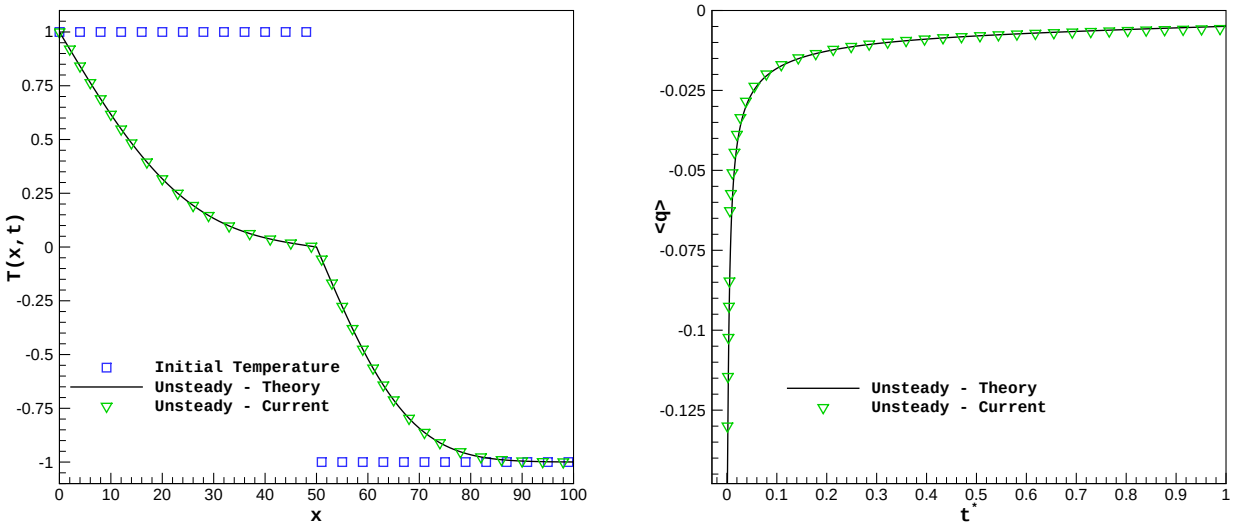

(a) (b)

FIG. 9: (a) Comparison of the temperature distribution at $t^* = 1$ along with initial temperature profile (square symbol) and (b) Comparison of the heat flux jump, $\langle q \rangle = q_v - q_l$, in the unsteady heat conduction problem between the current result (symbol) and the theory (line).

the liquid and vapor phases initially have a constant temperature, T_∞, which is less than saturation temperature, $T_{sat} = T_\infty + \Delta T_\infty$. The left boundary is a solid wall, which is kept at a constant temperature T_w higher than the saturation temperature, $T_w = T_{sat} + \Delta T_w$. The phase interface temperature is set to T_{sat} during the simulation. Initially, there is a thin layer of vapor in the system with 10 lattice grid size to initiate the phase change process. The initial temperature of liquid and vapor is set from the theoretical solution considering the initial vapor gap in the system. The simulation parameters in lattice units are listed in Table I. As the thermal profile evolves with time due to the temperature difference (ΔT_w), the phase interface feels the superheat that triggers the phase change process. The generated mass flow rate due to volume expansion at the phase interface pushes the liquid to exit from the right boundary and for that the vapor velocity becomes nearly zero ($u_v = 0$) during the phase change. A gradient free (open) boundary condition is applied at the right-side boundary in Fig. 10. The non-dimensional parameters defined in this problem are Stefan numbers based on vapor thermophysical properties $\mathrm{St}_v = c_{p_v} \Delta T_w / h_{fg}$ and liquid thermophysical properties $\mathrm{St}_l = c_{p_l} \Delta T_\infty / h_{fg}$. The theoretical solution for the phase interface

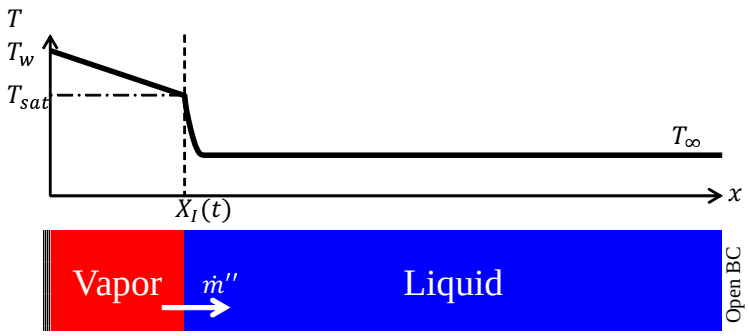

FIG. 10: A schematic of the two-phase Stefan problem with initial temperature profile.

TABLE I: Simulation parameters for benchmark problems (N_x is the lattice size).

	ρ_l/ρ_v	St_v	St_l	χ_v	χ_l	ΔT_w	ΔT_∞	N_x
Stefan Problem ($\rho_l/\rho_v \approx 1$)	1.5	1	1	0.01	0.01, 0.001	1	1	200
Stefan Problem ($\rho_l/\rho_v \gg 1$)	10, 100, 1000	1	0.005	0.001, 0.01, 0.1	0.0001	1	1	200
Sucking Interface Problem	50, 100, 200	0	0.004	0.006	0.006	0	1	500

location $X_I(t)$ and the transient vapor and liquid temperatures are given by [24]:

$$X_I(t) = 2\zeta\sqrt{\chi_v t}, \tag{48}$$

$$T_v(x,t) = T_w - \frac{\Delta T_w}{\mathrm{erf}\,(\zeta)}\mathrm{erf}\left(\frac{\zeta x}{X_I}\right), \tag{49}$$

$$T_l(x,t) = T_\infty + \frac{\Delta T_\infty}{\mathrm{erfc}\,(\zeta\rho_{vl}\chi_{vl})}\mathrm{erfc}\left(\frac{\zeta x\chi_{vl}}{X_I} - \zeta\chi_{vl}\,(1-\rho_{vl})\right), \tag{50}$$

where $\chi_v = k_v/(\rho_v c_{p_v})$ is the thermal diffusivity of vapor, $\chi_{vl} = \sqrt{\chi_v/\chi_l}$, $\rho_{vl} = \rho_v/\rho_l$, erf () is the error function, erfc () is the complementary error function $\mathrm{erfc}\,(x) = 1 - \mathrm{erf}\,(x)$ and parameter ζ is the solution of the following transcendental equation [24]:

$$\frac{\mathrm{St}_v}{\zeta e^{\zeta^2}\mathrm{erf}\,(\zeta)} - \frac{\mathrm{St}_l}{\zeta\rho_{vl}\chi_{vl}e^{(\zeta\rho_{vl}\chi_{vl})^2}\mathrm{erfc}\,(\zeta\rho_{vl}\chi_{vl})} = \sqrt{\pi}. \tag{51}$$

Considering the fact that the theoretical solution assumes no initial vapor profile in the system, the time variable t and the phase interface location $X_I(t)$ in Eqs. (48) and (49) are modified based on the initial phase interface location $X_I(0) = 10$.

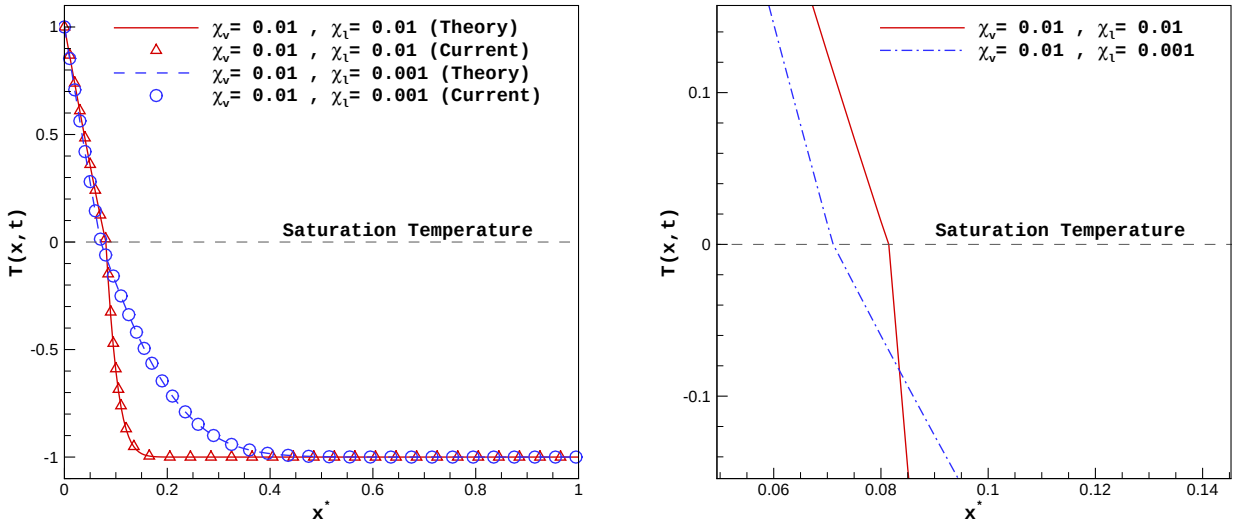

(a) (b)

FIG. 11: Comparison of the temperature distribution in the two-phase Stefan problem with small density effect ($\rho_l/\rho_v = 1.5$) between the LBE result (symbol) and the theory (line) for different thermal diffusivity ratios and (b) the sharp profile of the temperature across the phase interface.

1. *Effect of Thermal Diffusivity ($\rho_l/\rho_v = 1.5$)*

First, the density ratio is set to $\rho_l/\rho_v = 1.5$ and the effect of thermal diffusivity is considered. The physical parameters needed to set up the simulations are listed in Table I. In Fig. 11a, the temperature distribution at time $t^* = 0.2$ is compared to theoretical results for two different thermal diffusivity ratios, $\chi_v/\chi_l = 1$ and 10. A close look at the temperature profile at the phase interface in Fig. 11b confirms its sharp distribution. The thermal boundary layer in the liquid-side of the phase interface is thinner in case of smaller thermal diffusivity ratio ($\chi_v = \chi_l$). Additionally, the comparison of the phase interface movement between the LBE and theoretical results for both thermal diffusivity ratios is depicted in Fig. 12 in which they show an excellent agreement. For the unit thermal diffusivity ratio ($\chi_v = \chi_l$), the phase interface moves faster because the interfacial mass flux is larger. This is obvious from Fig. 11a where the temperature profile in the liquid-side is more steep for unit thermal diffusivity ratio, resulting in a larger heat flux jump at the phase interface.

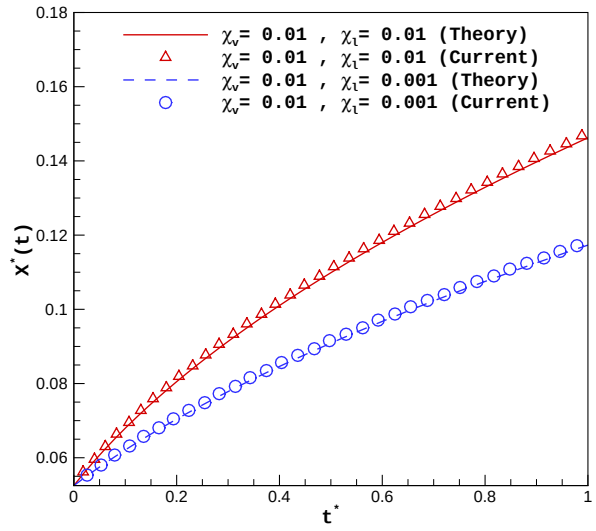

FIG. 12: Comparison of the phase interface location in the two-phase Stefan problem with small density effect ($\rho_l/\rho_v = 1.5$) for different thermal diffusivity ratios.

2. Effect of Density ($\rho_l/\rho_v \gg 1$)

In Fig. 13a, the LBE result for phase interface location is compared with the theoretical solution for three density ratios ρ_l/ρ_v=10, 100, and 1000. The non-dimensional time is $t^* = t/t_s$ and the non-dimensional phase interface location is $X^* = X_I/N_x$ where t_s is the total simulation time in lattice units and N_x is the lattice grid size in x-direction. The surface tension and phase interface thickness are $\sigma = 10^{-3}$ and $D = 5$ for all cases, respectively. The bulk energy constant and gradient parameter for density ratios $\rho_l/\rho_v = 10, 100, 1000$ are $\beta = 0.0036, 0.0024, 0.0024$ and $\kappa = 0.0092, 0.0076, 0.0075$, respectively. As can be seen in this figure, the simulation results are in good agreement with theory. Therefore, it is fair to conclude that even for a large density ratio up to 1000, the model is capable of correct prediction of the phase interface location meaning the diffusion term in the energy equation is accurately treated. As the phase interface moves away from the wall, it experiences a weaker temperature gradient and slows down. This is obvious from the slope of the curves in Fig. 13a. At any given time in Fig. 13a, the phase interface moves faster for larger density ratios.

The vapor phase remains stationary during the simulation but the liquid phase is pushed to the right with a constant velocity calculated from Eq. (15) as $u_l = u_I(1 - \rho_v/\rho_l)$ where u_I is the velocity of the phase interface. In Fig. 13b, the liquid velocity profiles are plotted

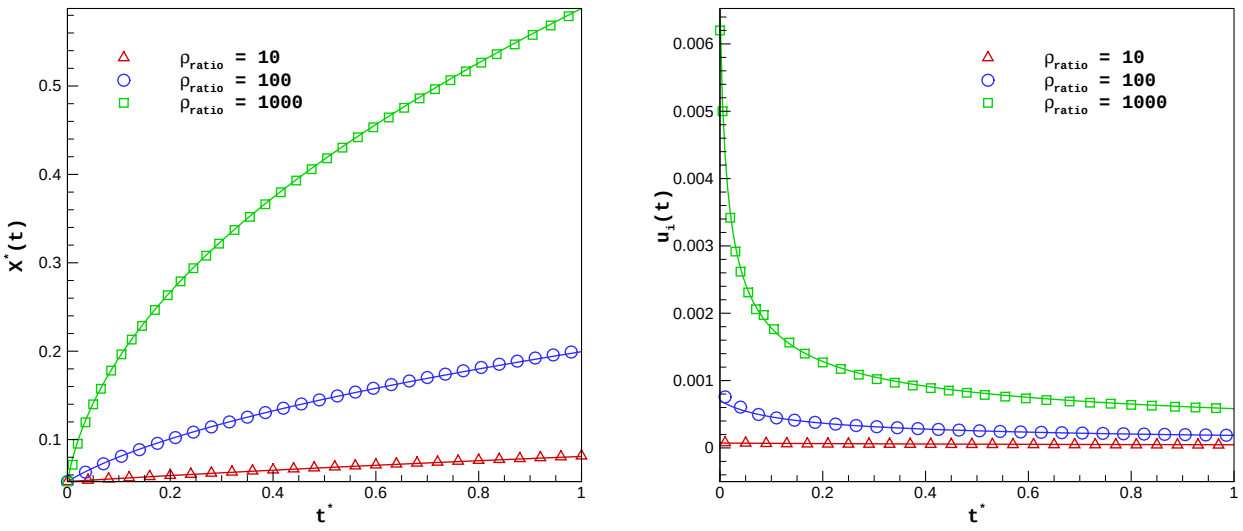

(a) (b)

FIG. 13: Comparison of (a) the phase interface location and (b) the liquid velocity (u_l) in the two-phase Stefan problem between the LBE result (symbols) and the theoretical solution (lines) [24] for different density ratios.

for three different density ratios $\rho_l/\rho_v = 10$, 100, and 1000. We found a good agreement in Fig. 13b between the LBE result and theoretical solution as well. The liquid velocity at the right boundary increases with the increasing density ratio.

The temperature profiles with a sharp distribution at the phase interface are shown in Fig. 14a for three density ratios of $\rho_l/\rho_v = 10$, 100, and 1000 at $t^* = 0.5$. The LBE results match well with theory and all temperature profiles exhibit a sharp distribution at the phase interface. Additionally, the phase interface with a larger vapor-to-liquid density ratio moves faster. The temporal evolution of the heat flux jump at the phase interface is plotted in Fig. 14b, where it shows a decreasing behavior in time for all density ratios. As the phase interface moves away from the left wall, the temperature slope decreases at the phase interface which results in a reduced heat flux jump. Since the heat flux jump is calculated at a moving phase interface, a small fluctuation in the numerical results around the theory is expected.

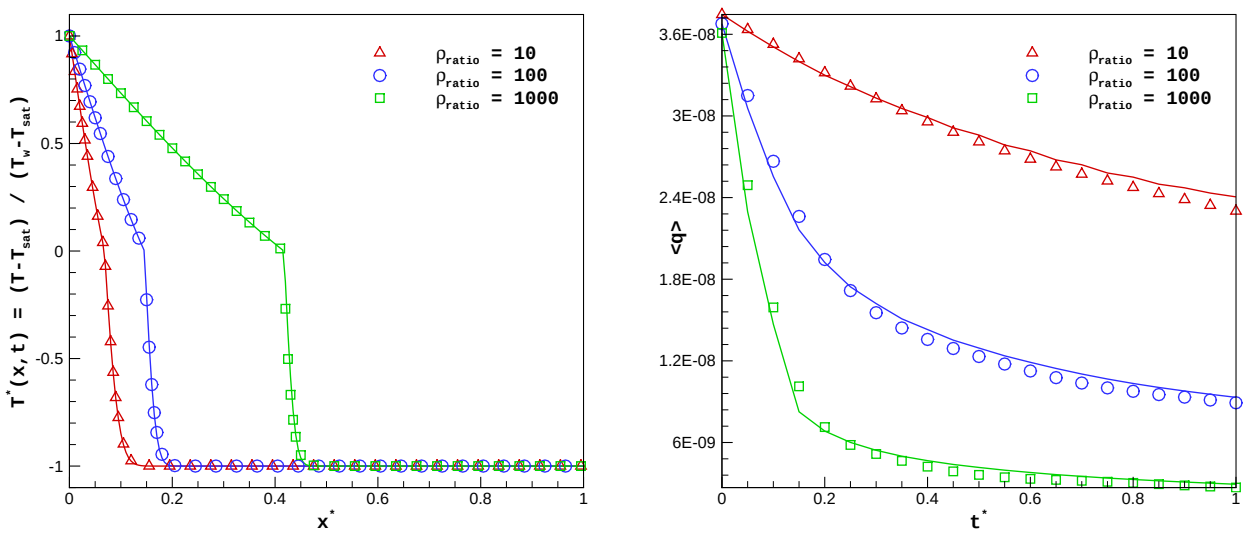

(a) (b)

FIG. 14: Comparison of (a) the non-dimensional temperature profiles at $t^* = 0.5$ and (b) the temporal evolution of the heat flux jump in the two-phase Stefan problem between the LBE result (symbols) and the theoretical solution (lines) [24] for different density ratios.

3. Effect of Phase Interface Thickness

One important parameter in simulations is the phase interface thickness D. In Fig. 15, the temporal evolution of the phase interface location is shown for different phase interface thicknesses ($D = 4, 5$, and 6) with a fixed density ratio of 100. The effect of phase interface thickness on the location of the phase interface is negligible. Therefore, it is kept constant ($D = 5$) for all density ratios in this study, while in [18], the phase interface thickness was dependent on a density ratio.

4. Convergence Test

In order to test the convergence of the model towards the sharp interface limit, the non-dimensional phase interface location $X^*(t)$ is plotted against the non-dimensional time t^* for three initial vapor layer thicknesses ($X(0) = 10, 20$, and 40) in Fig. 16a. Since the phase interface location changes with square root of time in Eq. 48, the total simulation time as well as the lattice size are changed based on the initial vapor layer thickness. In all cases, the initial vapor layer thickness is 5% of the total lattice size. The solution converges to the

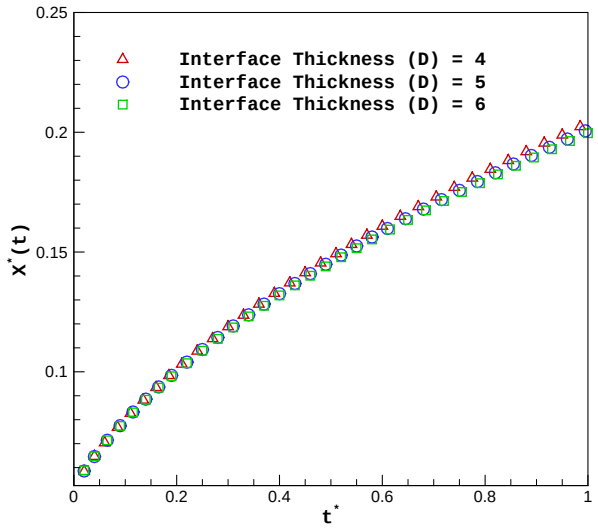

FIG. 15: Comparison of the phase interface location in the two-phase Stefan problem for different phase interface thicknesses at $\rho_l/\rho_v = 100$.

theoretical solution as the initial vapor layer thickness increases. Since the system initially is slightly away from the equilibrium, the mass flow rate calculation has a smaller error if the initial temperature gradient at the phase interface is less steep and the mass flow rate is small. The slope of initial temperature profile at the phase interface decreases as the initial vapor layer thickness increases.

In Fig. 16b, a convergence test is done for different thermal diffusivities of $\chi = 0.001, 0.002,$ and 0.004 at a density ratio of 100. In all cases, the thermal diffusivity of vapor is larger than the liquid one by two order of magnitude, $\chi_v/\chi_l = 100$. The error between the theoretical solution and LBE method decreases as the thermal diffusivity decreases. The reason behind this is the explicit temporal discretization of the macroscopic energy equation. The current solution (t^n) in the discretization scheme is dependent on previous solution (t^{n-1}) and obviously the error increases when there is a large jump at phase interface location. When larger thermal diffusivity intensifies the boiling rate, the phase interface jump between two consecutive time steps increases and the error compared to theoretical results increases as well.

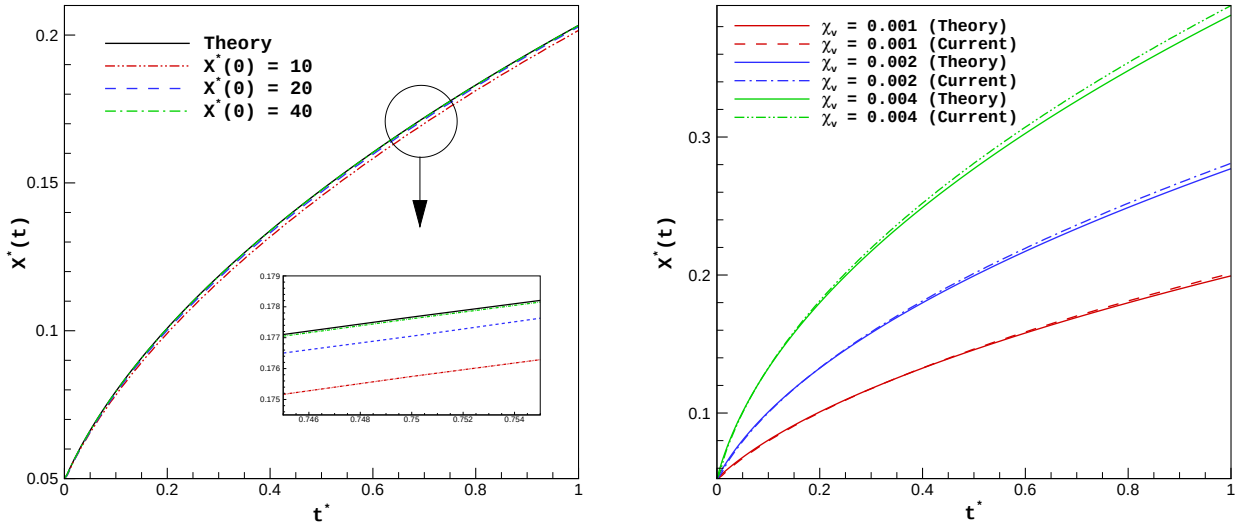

(a) (b)

FIG. 16: Convergence test toward sharp interface limit for the interface location based on (a) different initial vapor layer thicknesses $X(0) = 10, 20, 30$, and 40 and (b) different thermal diffusivities $\chi = 0.001, 0.002, 0.004$ in the two-phase Stefan problem.

C. Two-Phase Sucking Interface Problem

The next one-dimensional validation benchmark is defined by slightly modifying the first case in section III B in terms of the initial temperature distribution. A schematic diagram of the problem along with an initial temperature distribution is depicted in Fig. 17. The left wall is maintained at lower temperature compared to saturation temperature ($T_{sat} = T_w + \Delta T_w$) and the right boundary is kept at $T_\infty = T_{sat} + \Delta T_\infty$. The only difference is that the thin thermal layer in the interfacial region (located mostly on the liquid-side) controls the phase interface velocity. This problem is very close to the real boiling situation where there is a thin thermal boundary layer in the liquid-side of the phase interface. Due to the volume expansion of liquid, the phase interface velocity is expected to be higher than that in the first benchmark [13]. The theoretical solutions of the phase interface location and liquid temperature are [38]:

$$X_I(t) = 2\frac{\zeta}{\rho_{vl}}\sqrt{\chi_v t}, \tag{52}$$

$$T_v(x,t) = T_w + \frac{\Delta T_w}{\text{erf}\,(\zeta/\rho_{vl})}\text{erf}\left(\frac{\zeta x}{X_I \rho_{vl}}\right), \tag{53}$$

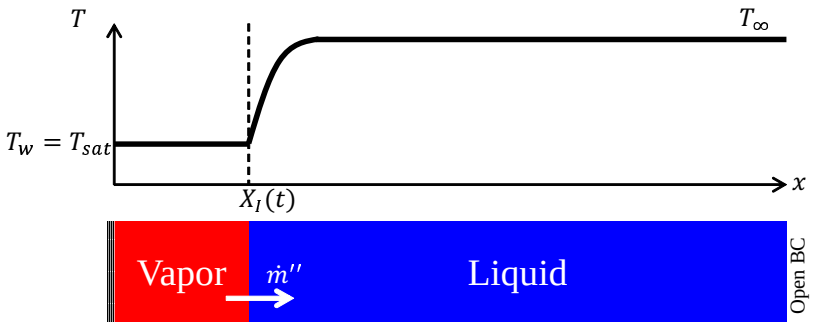

FIG. 17: A schematic of the two-phase sucking interface problem and the initial temperature profile.

$$T_l(x,t) = T_\infty - \frac{\Delta T_\infty}{\text{erfc}\,(\zeta\chi_{vl})}\text{erfc}\,\left(\frac{\zeta x\chi_{vl}}{X_I\rho_{vl}} - \zeta\chi_{vl}\frac{1-\rho_{vl}}{\rho_{vl}}\right), \tag{54}$$

where ζ is the solution of the following transcendental equation [38]:

$$e^{(\zeta/\rho_{vl})^2}\text{erf}\,(\frac{\zeta}{\rho_{vl}})\left[\zeta - \frac{\text{St}_l}{\sqrt{\pi}\chi_{vl}}\frac{e^{-(\zeta\chi_{vl})^2}}{\text{erfc}\,(\zeta\chi_{vl})}\right] = -\frac{\text{St}_v\rho_{vl}}{\sqrt{\pi}}. \tag{55}$$

Parameters $\text{St}_l = c_{p_l}\Delta T_\infty/h_{fg}$ and $\text{St}_v = c_{p_v}\Delta T_w/h_{fg}$ are the Stefan numbers based on liquid and vapor thermophysical properties. The initial temperature profile is calculated from Eqs. (53) and (54). The simulation parameters for this problem in lattice units are listed in Table I. The wall superheat is set to zero in this simulation ($\Delta T_w = 0$). The time evolution of the phase interface location is compared with the theoretical solution for three different density ratios (ρ_l/ρ_v = 50, 100, and 200) in Fig. 18. A good agreement is found between the LBE results and theoretical solutions. The rate of the phase interface velocity increase is more pronounced compared to the two-phase Stefan problem in section III B due to the placement of the thermal boundary layer in the liquid-side of the phase interface.

The initial thermal layer in the interfacial region tends to spread as the simulation progresses. However, this effect is minimized by sucking the thermal layer toward the phase interface [3], which keeps the thermal layer thin (Fig. 19) during the simulation. Fig. 20 shows a scaling relation pertaining to the relationship between the calculated non-dimensional phase interface displacement and the Stefan number after a fixed number of iterations. It shows that the phase interface moves faster with increasing Stefan number and the phase interface displacement is scaled with the square root of the Stefan number by $\Delta X_I/X_I(0) \sim \text{St}_l^{0.5}$. The curve is shown by a linear profile in Fig. 20 since it is plotted in log-log scale.

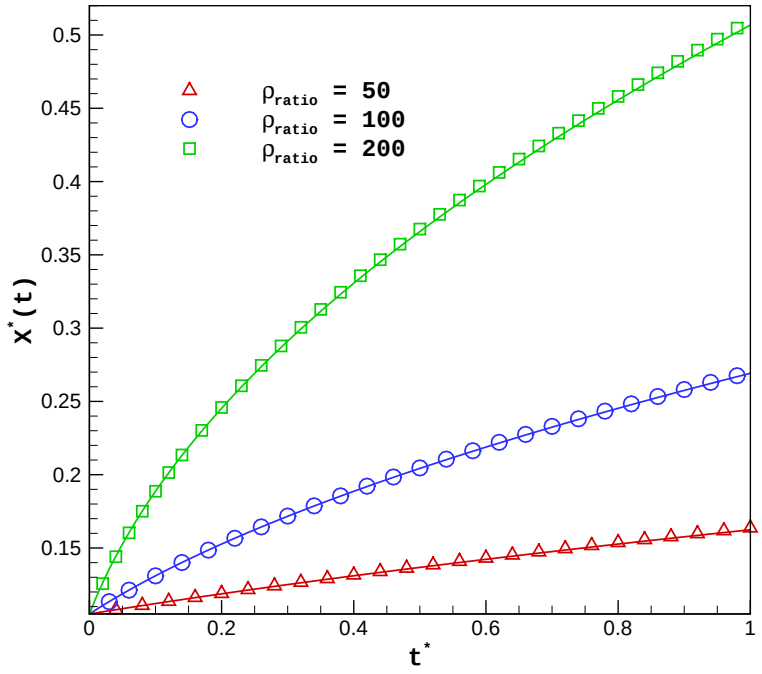

FIG. 18: Comparison of the phase interface location in the two-phase sucking interface problem between the LBE result (symbols) and the theoretical solution (lines) [13] for different density ratios.

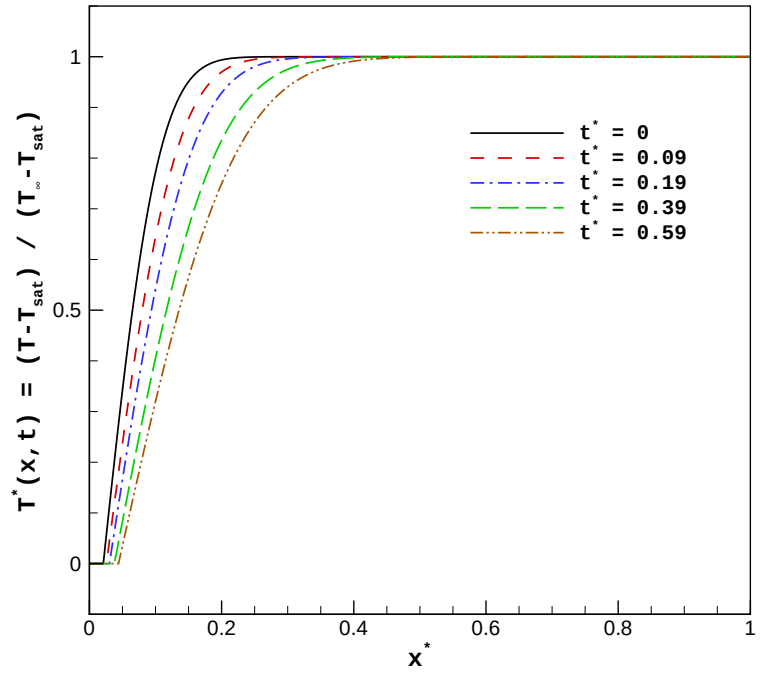

FIG. 19: The temperature profile at different times in the two-phase sucking interface problem at $\rho_l/\rho_v = 100$.

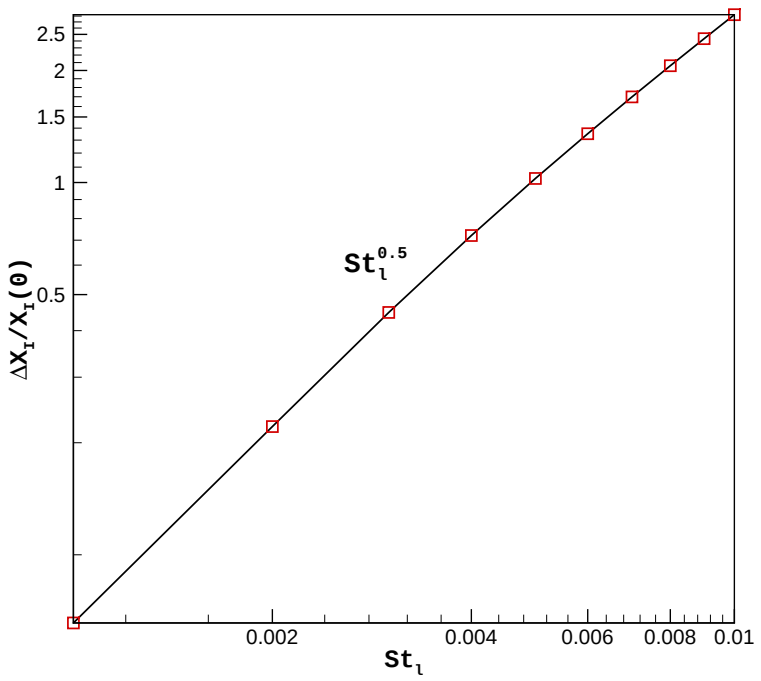

FIG. 20: The scaling relation between the calculated non-dimensional phase interface displacement and Stefan number after a fixed number of iterations in the two-phase sucking interface problem.

D. Liquid Droplet Evaporation

In the first three benchmark problems, the surface tension force did not play a role in the evolution of the phase interface. To test the present model with the effect of surface tension force, a two-dimensional liquid droplet evaporation problem is simulated.

In Fig. 21a, a circular droplet with an initial radius R_0 is placed at the center of the computational domain. All the boundary conditions are specified as gradient free boundaries to allow the vapor, generated due to volume expansion at the phase interface, to exit freely and without any disturbance.

The initial liquid temperature $T_{l,0}$ and the vapor temperature $T_{v,0}$ are set to the saturation temperature T_{sat} and T_∞, respectively. During the simulation, the droplet temperature as well as the phase interface temperature are kept constant at T_{sat} and the temperature at the boundaries is kept higher than the saturation temperature $T_\infty = T_{sat} + \Delta T$.

In Fig. 21b, the droplet radii at different simulation times ($t^* = 0$, 0.29, 0.67, and 1) are shown. The initial circular droplet shape remains circular at later times which shows that

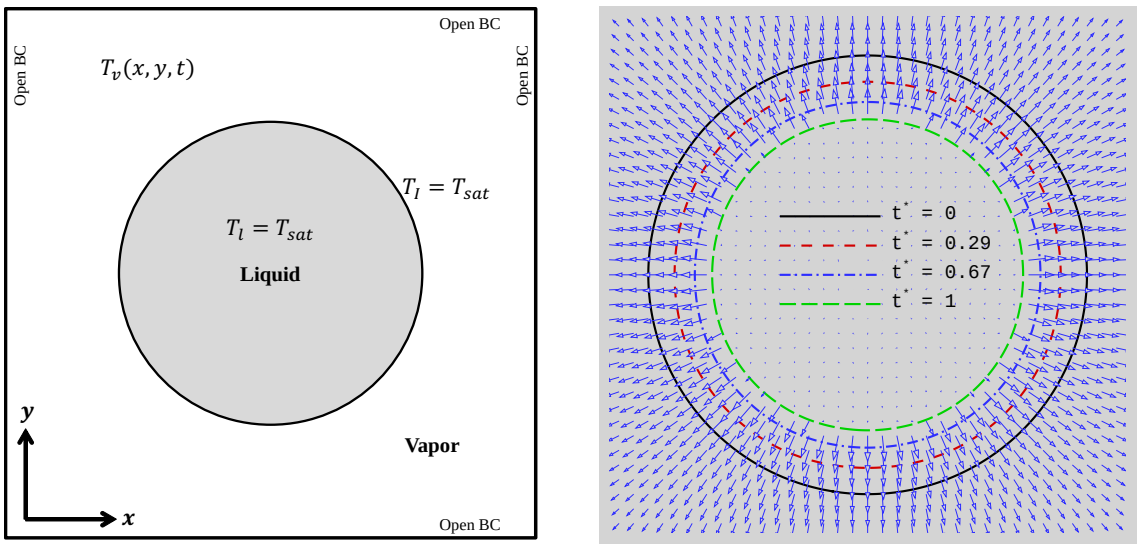

(a) (b)

FIG. 21: (a) A schematic diagram of the droplet evaporation. (b) Transient radius of the droplet at $t^* = 0$, 0.29, 0.67, and 1 and velocity vectors around the evaporating droplet.

the phase change model is consistent with the volumetric surface tension formulation and is direction independent. To further prove this point, velocity vectors around the droplet are shown in Fig. 21b. The velocity vectors generated by interfacial mass flow are all in the radial direction which shows the uniformity of mass flow rate in that direction.

To investigate the mesh independent solution, the evaporation of a liquid droplet with five different initial radii of R_i = 12.5, 25, 50, 75, and 100 (lattice unit) are simulated and the results are shown in Fig. 22. The final shape of the liquid droplet when the non-dimensional transient radius meets the $R^*(t)^2 = 0.5$ relation is provided in Fig. 22a where $R^*(t) = R(t)/R_0$. The non-dimensional transient radius, $R^*(t)$, at each time is shown in Fig. 22b. From the results of both Fig. 22a and Fig. 22b, it is clear that the difference between the cases with initial radius of $R_0 = 50$, 75, and 100 is negligible. The initial radius of $R_0 = 75$ is considered for the rest of simulations on the droplet evaporation study to attain the most accurate result.

The Young-Laplace equation links the pressure difference across the phase interface to the phase interface shape between two fluids. Although it is essentially important in the study of static capillary surfaces, it is shown in [39] that in the case of droplet evaporation this relation also holds under specific circumstances such as slow evaporation rate. This

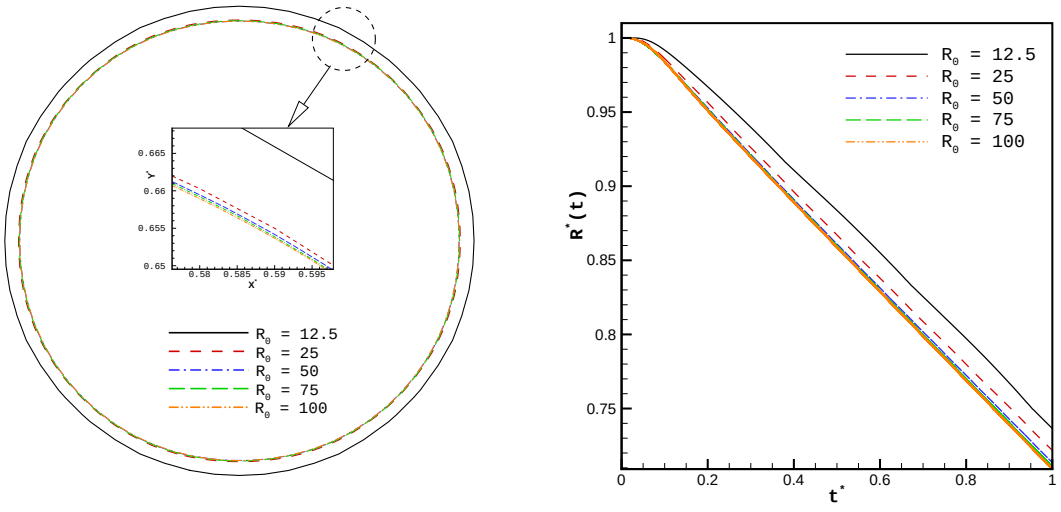

(a) (b)

FIG. 22: (a) Mesh study in the droplet evaporation problem. (b) Transient radius of the droplet for five different initial radii.

can be satisfied by having a very slow phase change process where the thermal diffusivity of vapor is set to $\chi_v = 0.01$ and the Ja number is set to Ja $= 1.0$ in lattice units. The Ja number is defined as Ja $= c_{p_v}\Delta T/h_{fg}$. The pressure jump across the phase interface is related to the phase interface curvature by:

$$\Delta p = p_i - p_o = \frac{\sigma}{R(t)}, \tag{56}$$

where p_i and p_o are the pressures inside and outside of the curved phase interface, respectively. After the initial waves and disturbances due to unequilibrium state of the flow, the pressure inside and outside of the droplet becomes almost constant. The result of the Young-Laplace equation validation is shown in Fig. 23. The LBE result agrees well with the theoretical relation in Eq. (56). Another simulation with a higher evaporation rate ($\chi_v = 0.05$ and Ja $= 1.0$) is shown in Fig. 23. Since the rate of evaporation in this case is higher than the case with $\chi_v = 0.01$, the deviation from Laplace law is more pronounced. Additionally, the numerical results slightly deviate from Laplace law as the radius decreases in both evaporation rates ($\chi_v = 0.01$ and 0.05). The most likely explanation is non-uniformity in pressure inside the droplet. The pressure in the interfacial area has small fluctuations and will affect the inside pressure (p_i) calculation. Finally, the good agreement with the theory shows that mechanical equilibrium is reached earlier than the thermal equilibrium

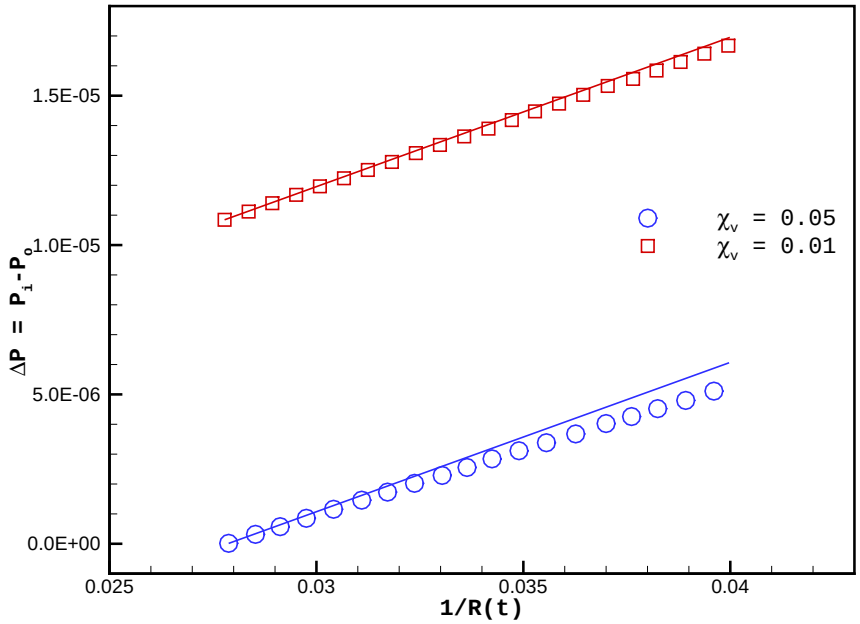

FIG. 23: Comparison of the Young-Laplace law for the evaporating droplet between the LBE result (symbol) and the theory (line) for two different rates of evaporation corresponding to $\chi_v = 0.01$ and 0.05.

in the case of a slow phase change process. The phase interface velocity is very small since the rate of evaporation is very low and it is in the order of 10^{-5} for both thermal diffusivity cases to ensure the mechanical equilibrium during evaporation.

In Fig. 24, the d^2 law investigation for droplet evaporation is carried out for different Ja numbers ranging from 0.25 to 1.0. For all Ja numbers which correspond to different rates of evaporation, the d^2 law is satisfied since the $(D/D_0)^2$ changes linearly as simulation goes forward in time. At any given time, the rate of evaporation is higher for a larger Ja number.

Effect of different surface tension and relaxation parameters on transient radius of the droplet during evaporation is studied for three different Laplace numbers ($\mathrm{La} = \sigma\rho_l D_0/\mu_l^2$) in Fig. 25. In each case, all other parameters were kept constant except the variable parameter which is surface tension in Fig. 25a and relaxation parameter in Fig. 25b. In Fig. 25a, the surface tensions of $\sigma = 0.0005, 0.0008, 0.001$ corresponds to Laplace numbers of $\mathrm{La} = 1.80, 2.88, 3.60$, and the relaxation parameters of $\tau = 0.05, 0.1, 0.5$ corresponds to $\mathrm{La} = 288, 72, 2.88$ in Fig. 25b, respectively. For both variable surface tension and variable relaxation parameter, the results are almost the same and the difference is negligible. This observation matches our expectation since the rate of evaporation is not affected by surface

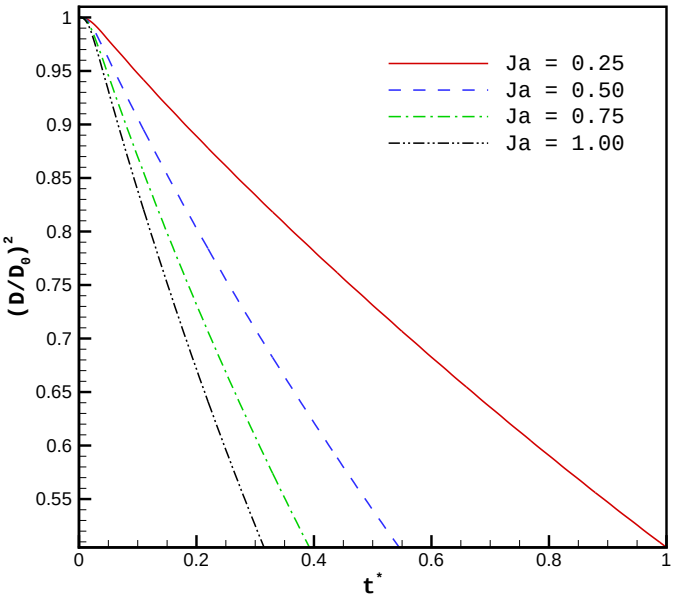

FIG. 24: The investigation of the d^2 law in droplet evaporation problem for four different Ja numbers of Ja = 0.25, 0.5, 0.75, and 1.0.

tension and relaxation parameter only.

E. Vapor Bubble Growth in Superheated Liquid

The three-dimensional radial growth of a vapor bubble inside a superheated liquid is the most reliable benchmark for the verification of a boiling model since the theoretical solution incorporates the radii of curvature and all thermophysical properties involved in the physics of problem. This benchmark is very close to a real boiling situation where a tiny vapor bubble starts to grow in a superheated liquid. An initially saturated vapor bubble (T_{sat}) placed inside a superheated liquid ($T_\infty = T_{sat} + \Delta T$) experiences a thin thermal boundary layer around its phase interface as depicted in Fig. 26. The schematic of the problem and the temperature profile are shown in this figure and the thermal boundary layer is sketched with a light blue donut shape around the vapor bubble. The thin thermal boundary layer activates phase change at the liquid-vapor interface and the radius of curvature, $R(t)$, increases with time.

The theoretical solution of this problem is provided in [40] and the transient radius during

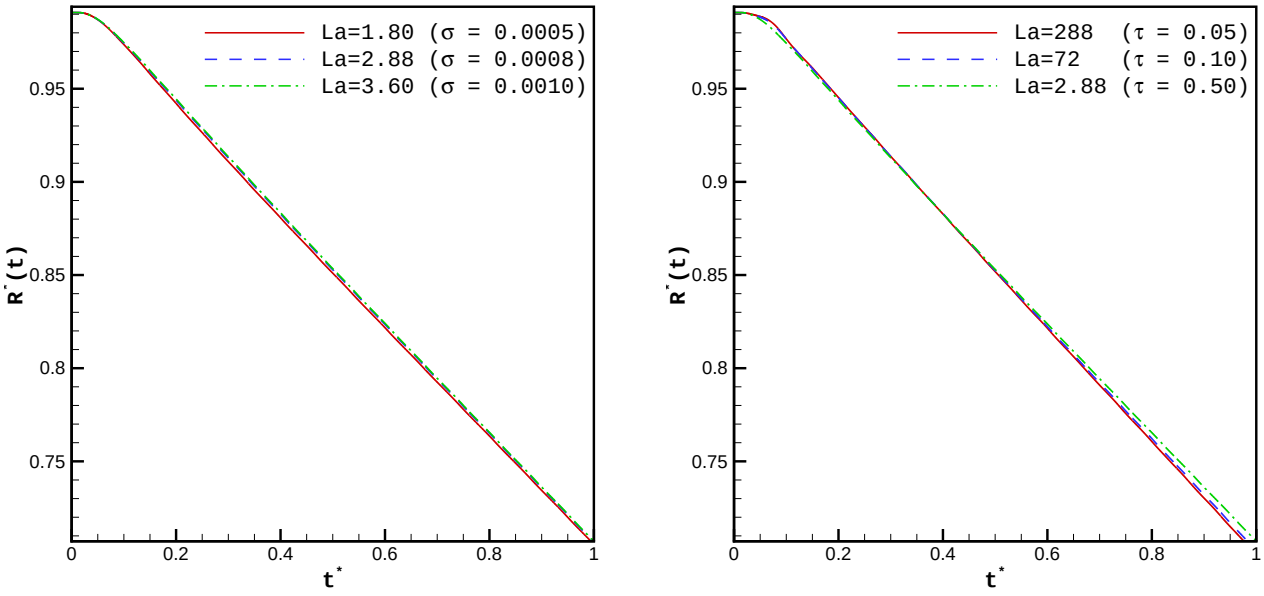

(a) (b)

FIG. 25: Effect of (a) surface tension (b) relaxation parameter corresponding to three different Laplace numbers ($\mathrm{La} = \sigma\rho_l D_0/\mu_l^2$) on transient radius of the droplet during evaporation.

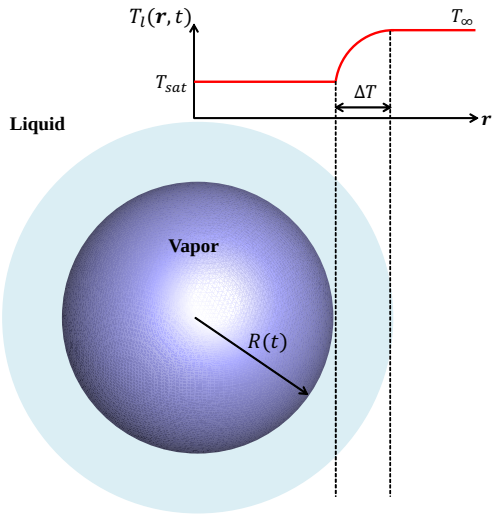

FIG. 26: A schematic of the vapor bubble growth problem in a superheated liquid and the temperature distribution in radial direction where the donut shape with light blue color represents the thermal boundary layer around the vapor bubble.

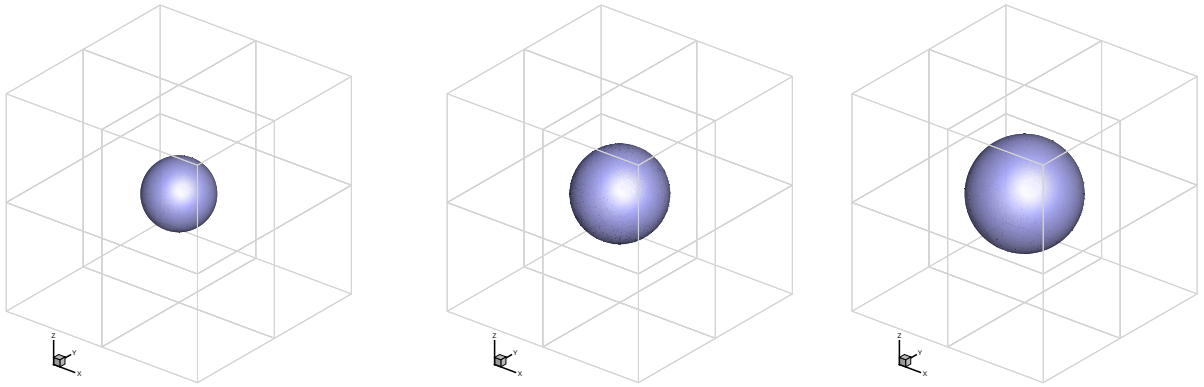

(a) (b) (c)

FIG. 27: Transient shape of the vapor bubble at different simulation times (a) $t^* = 0$, (b) $t^* = 0.5$, and (c) $t^* = 1.0$.

the boiling is calculated by,

$$R(t) = \zeta\sqrt{4\chi_l t}, \tag{57}$$

where the ζ is the solution of the following transcendental equation [40],

$$2A\rho_{vl}\zeta^2 \int_0^1 e^{-\zeta^2\left((1-s)^{-2}-2(1-\rho_{vl})s-1\right)}ds - 1 = 0. \tag{58}$$

The parameter A in Eq. (58) is defined as $A = \mathrm{Ja}_l/(1+\mathrm{Ja}_l-\mathrm{Ja}_v)$, where $\mathrm{Ja}_l = c_{p_l}\Delta T/h_{fg}$ and $\mathrm{Ja}_v = c_{p_v}\Delta T/h_{fg}$ are Ja numbers based on liquid and vapor properties, respectively. The integral relation in Eq. (58) is solved numerically in order to find the ζ constant for each simulation. In theory, a vapor bubble can start to grow from a zero radius. However, a vapor bubble with a non-zero initial radius is considered in current simulation and the initial temperature from the theoretical solution is prescribed in the computational domain. The theoretical equation for temperature distribution in the computational domain as a function of the radii of curvature is defined as [40],

$$T(r) = \begin{cases} T_\infty - 2A\Delta T\rho_{vl}\zeta^2 \int_{1-\frac{R(t)}{r}}^1 e^{-\zeta^2\left((1-s)^{-2}-2(1-\rho_{vl})s-1\right)}ds, & \text{if } r > R(t) \\ T_{sat}, & \text{if } r \leq R(t) \end{cases}. \tag{59}$$

The calculation of the initial temperature distribution in the radial direction is carried out using the same numerical approach used in derivation of ζ in Eq. (58). In the Cartesian lattice grid, the radial position is defined as $r = \sqrt{(x-x_c)^2+(y-y_c)^2+(z-z_c)^2}$, where x_c, y_c, and z_c are the coordinates of the center of computational domain. Only $1/8^{th}$ of the

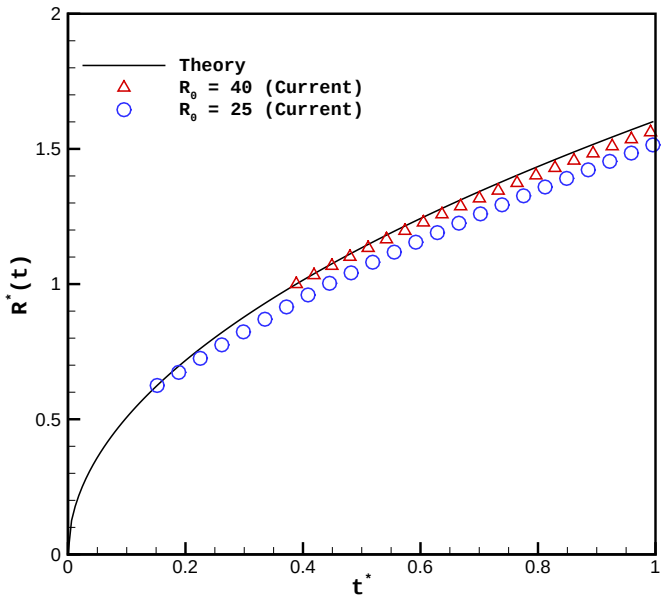

FIG. 28: Comparison of the transient radius in the vapor bubble growth problem between the LBE result (symbols) and the theoretical solution (lines) [40].

domain is solved due to its symmetrical properties in x, y, and z directions. The initial temperature profile is extracted from the Eq. (59) at $R(t) = R_0$, where R_0 is the initial radius of the vapor bubble.

The simulation parameters in lattice unit are set to $R_0 = 40$, $\rho_{vl} = 0.066$, $\mathrm{Ja}_v = 0.001$, $Ja_l = 0.1$, $\chi_v = 0.04$, $\chi_l = 0.004$, $\sigma = 0.001$, and $\Delta T = 1$. The size of computational domain is set to $n_x \times n_y \times n_z = 128 \times 128 \times 128$ which is only $1/8^{th}$ of the full domain. The snapshots of the vapor bubble at different simulation times are investigated in Fig. 26. The perfectly spherical shape of the vapor bubble at different times in this figure is consistent with uniform treatment of the interfacial source term at the phase interface.

In Fig. 28, the transient radius of vapor bubble, $R(t)$, is compared against the theoretical solution presented in Eq. (57). Two initial radii are considered ($R_0 = 25$ and $R_0 = 40$) in the simulations while all other parameters are kept constant. The initial radius of $R_0 = 25$ and $R_0 = 40$ corresponds to a computational domain with lattice size of 64^3 and 128^3, respectively. Again, the size of the computational domain is only $1/8^{th}$ of the problem schematic shown in Fig. 26. The small difference between the LBE results and the theoretical solutions is due to the thin thermal boundary layer at the phase interface. This error decreases by refining the computational grid and this task is done by increasing the size of

the computational domain in the LBE method. Additionally, the thermal boundary layer is resolved better in the case of a finer mesh. In both initial radius cases, the error between the theory and LBE method increases as the vapor bubble grows in size. This behavior is linked to the boundary condition at the open sides. The hydrodynamic boundary condition at open sides is set to gradient free to let the liquid exit freely in the radial direction and the thermal boundary condition is set to constant T_∞ temperature to mimic the theoretical setup. As the temperature profile evolves in time, it deviates from T_∞ at computational sides and it does not follow the constant T_∞ temperature at the infinity in the case of theoretical solution. Again, this error can be significantly decreased by refining the computational grid.

The refinement of the computational grid and the search for a mesh independent solution are done in a two-dimensional vapor bubble growth problem since it is very time consuming in three-dimensional case. The results are presented in Fig. 29 where four different radii of curvature ($R_0 = 20$, 30, 40, and 50) are considered. From Eq. (57), the simulation time scales with $t \propto R^2/\chi_l$. Therefore, by doubling the initial vapor bubble radius, the thermal diffusivity of liquid is quartered in order to keep the same simulation time. As shown in Fig. 29, the solution converges as the initial radius of vapor bubble increases. There is a negligible difference between the results of radius $R_0 = 40$ and 50. Therefore, a vapor bubble with initial radius of $R_0 = 40$ in lattice unit is considered in this study.

In the three-dimensional vapor bubble growth problem, the radial distribution of temperature, velocity magnitude, density, and interfacial source term due to phase change are plotted in Fig. 30. The start and end points in Cartesian coordinate are (x_c, y_c, z_c) and (n_x, y_c, z_c), respectively. The velocity magnitude, density, and interfacial source term are shown in a separate vertical axis for the sake of clarification.

The thermal boundary layer on the liquid-side of the phase interface is clearly shown where temperature changes from T_{sat} to T_∞. The velocity experiences a jump across the phase interface as expected and the interfacial source term is non-zero only at phase interface.

F. Vapor Bubble Rising in Superheated Liquid

A vapor bubble rising in a superheated liquid under gravity is studied in this section in order to mimic a real boiling situation. The main difference in this problem compared to previous benchmarks is the fluid flow around the vapor bubble as it rises due to buoyancy

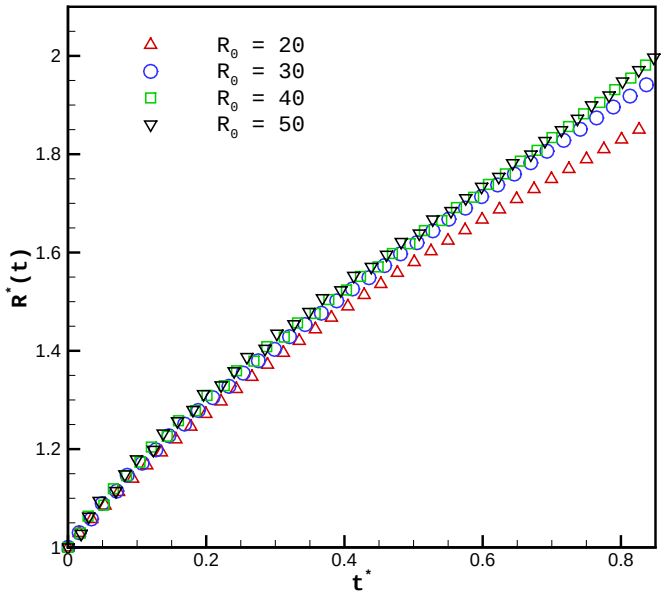

FIG. 29: Investigation of a mesh independent solution in a two-dimensional vapor bubble growth in a superheated liquid.

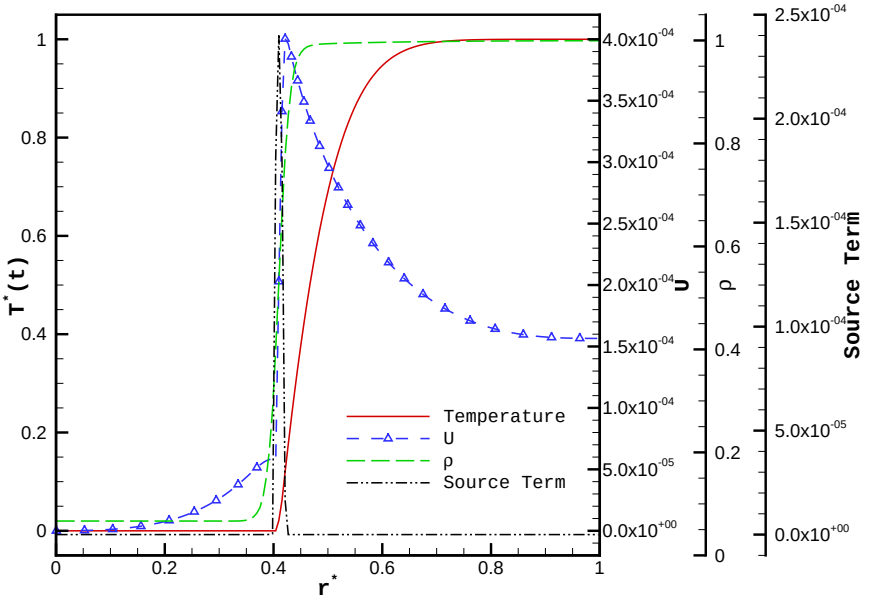

FIG. 30: Radial distributions of temperature, velocity magnitude (U), density (ρ), and interfacial source term across the phase interface at $t^* = 0.5$ in the vapor bubble growth problem..

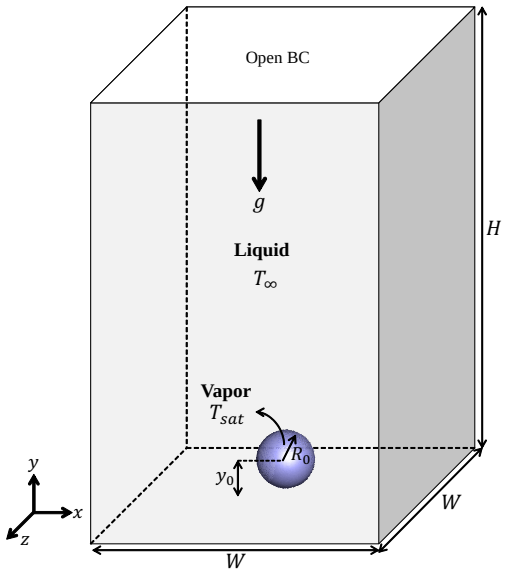

FIG. 31: A schematic of the three-dimensional vapor bubble rising in a superheated liquid problem.

force in a superheated liquid pool.

As depicted in Fig. 31, a vapor bubble at saturation temperature (T_{sat}) is placed at a vertical distance of y_0 from the bottom of a vertical channel filled with a superheated liquid (T_∞). The bottom and all sides of the computational domain are solid walls and no-slip boundary condition expect the top where it is set to an open/free boundary. The open/free boundary condition at top warrants a disturbance-free liquid exit or entrance from the computational domain. The size of the full computational domain is $W \times W \times H$ in lattice size. The geometrical parameters and thermophysical properties for this problem are $\rho_l/\rho_v = 100$, $\mu_l/\mu_v = 100$, $\mathrm{Ja}_v = 0.0005$, $\mathrm{Ja}_l = 0.05$, $\mathrm{Eo} = 4.95$, $\mathrm{Mo} = 0.095$, $\Delta T_\infty = 3.1$, $W = 200$, and $H/W = 3$ in lattice unit. The Eötvös number and the Morton number are defined as $\mathrm{Eo} = g(\rho_l - \rho_v)D^2/\sigma$ and $\mathrm{Mo} = \mu_l^4(\rho_l - \rho_v)g/\sigma^3\rho_l^2$, respectively. The superheat which is the difference between vapor saturation temperature and the liquid temperature is set to $\Delta T_\infty = 3.1$ in lattice unit. Therefore, the initial temperature of the vapor bubble is set to saturation temperature, T_{sat}, and the liquid pool is set to $T_\infty = T_{sat} + \Delta T_\infty$. The temperature at side walls and the bottom wall are kept at T_∞. The computational domain is divided into four equal parts due to symmetric behavior in x and z directions and only $1/4^{th}$ of the computational domain is considered for simulation to save in numerical simulation time.

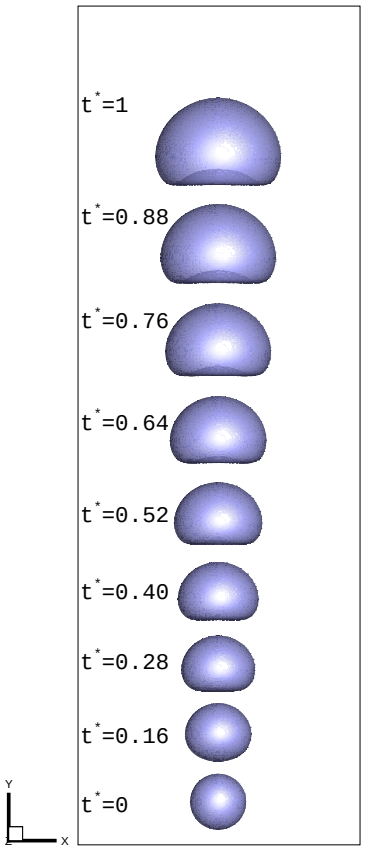

FIG. 32: Snapshots of the vapor bubble shapes at different simulation times $t^* = 0$, 0.16, 0.28, 0.40, 0.52, 0.64, 0.76, 0.88, and 1 in vapor bubble rising in superheated liquid problem.

As the simulation starts, the vapor bubble rises in the liquid pool due to buoyancy force and expands in size due to phase change at liquid-vapor phase interface. This problem is very challenging for calculation of the interfacial mass flow since the temperature is affected by the fluid flow around the vapor bubble. The snapshots of the vapor bubble at different times are shown in Fig. 32. As the vapor bubble rises in a liquid with higher density ($\rho_l/\rho_v = 100$), its profile deviates from the initial spherical shape. It shows a concave profile at vapor bubble top and a convex profile at the bottom before $t^* = 0.28$. However, as the vapor bubble vertical distance from the bottom wall increases, it lefts a wake and low-pressure area below it. The low-pressure area underneath the vapor bubble flattens its convex profile at bottom and it becomes flat around $t^* = 0.28$. The vapor bubble shape at bottom becomes concave past time $t^* = 0.40$ due to increasing low-pressure area. The snapshots in Fig. 32 are made

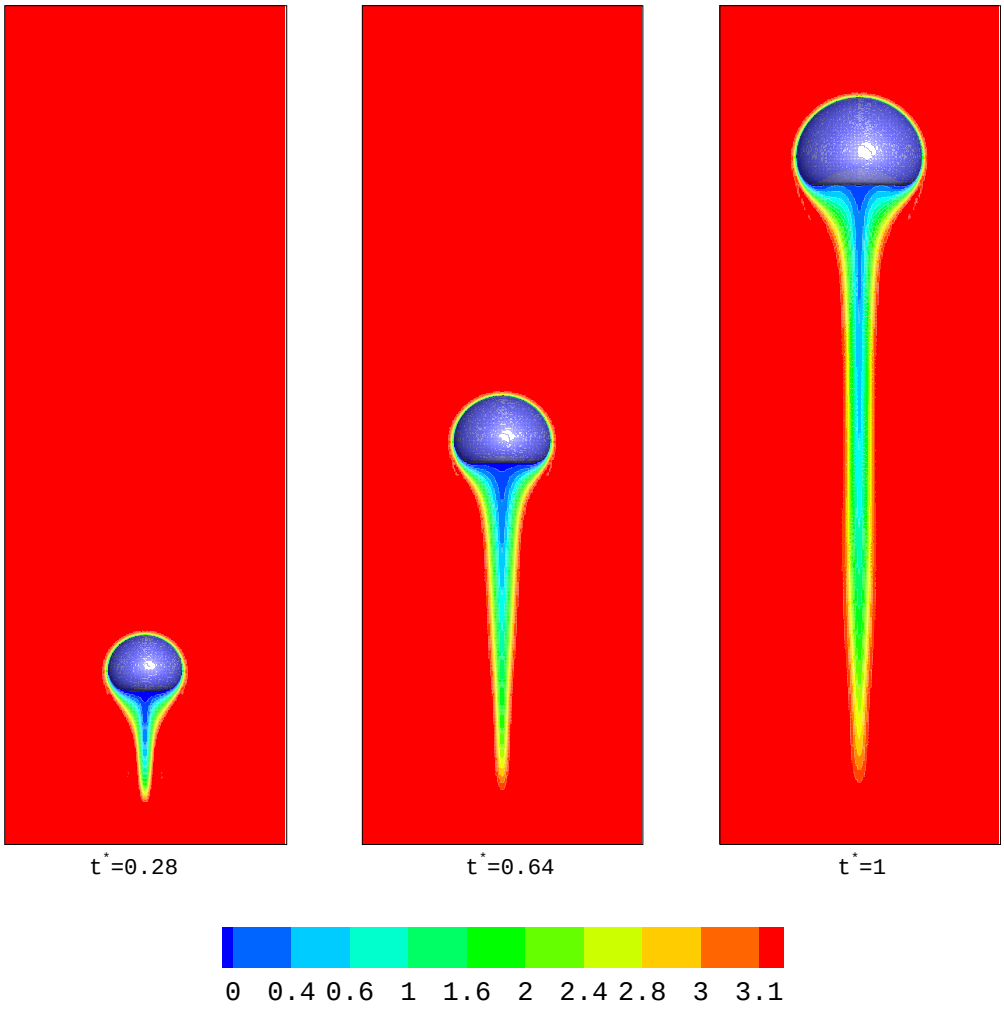

FIG. 33: Temperature contours at the mid-plane in z-direction along with the vapor bubble transient shape at three different times $t^* = 0.28$, 0.64, and 1 in vapor bubble rising in a superheated liquid problem.

transparent to clearly show the concave profile below the vapor bubble after $t^* = 0.40$. The smooth and curved surface of the vapor bubble indicates the correct treatment of the mass flow at liquid-vapor phase interface.

The temperature contour at the mid-plane in z-direction along with the vapor bubble transient shape at three different times ($t^* = 0.28$, 0.64, and 1) are shown in Fig. 33. The thermal boundary layer at the top part of the vapor bubble is thinner compared to that underneath. As the vapor bubble rises in the liquid pool, the liquid is pushed upward and it comes down from both sides of the vapor bubble. This motion of the superheated liquid

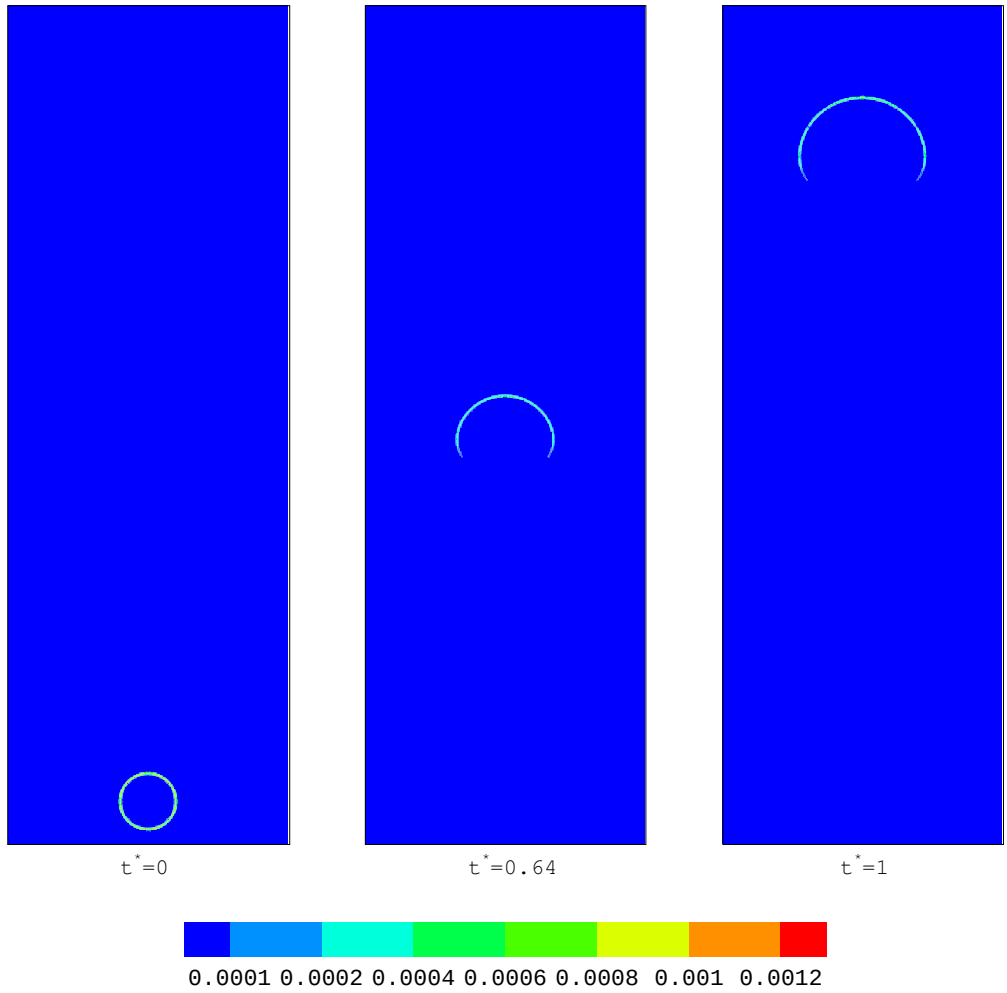

FIG. 34: The interfacial source term contours at the mid-plane in z-direction at three different times $t^* = 0$, 0.64, and 1 in vapor bubble rising in a superheated liquid problem.

replaces the saturated temperature area of the vapor bubble as it moves upward. Therefore, the convection heat transfer from superheated liquid to saturated area creates a needle-shaped and narrow region in temperature contours beneath the vapor bubble. This narrow region expands as the vapor bubble moves upward.

The upward motion of the bubble and the convection of the superheated liquid affects the temperature below the vapor bubble. Additionally, the lower temperature under the vapor bubble influences the interfacial mass flow due to decreased heat flux at the liquid-vapor phase interface. In Fig. 34, the contours of the interfacial source term defined in Eq. (1) are shown for $t^* = 0$, 0.64, and 1. The interfacial source term expands all around the vapor bubble at initial times but its distribution profile is changed as the vapor bubble rises in

the superheated liquid. The interfacial source term below the vapor bubble becomes almost zero and this region expands in size as the vapor bubble rises further.

IV. CONCLUDING REMARKS

In this paper, we aimed to present a new pressure evolution equation based lattice Boltzmann model to deal with phase change in single-component fluids for future applications to thermal management of micro-electronic devices. The macroscopic energy equation is spatially discretized and solved with 2nd-order accurate isotropic finite difference. A phase change model is embedded in the pressure evolution equation, which enforces near-incompressibility in the bulk phases and allows phase change in the interfacial region. The thermal parameters such as thermal conductivity and specific heat are sharp across the phase interface. The sharp interface treatment of macroscopic internal energy equation makes the model desirable for subcooled boiling applications since a full control over the phase interface temperature is available in the current model.

The LBE results showed excellent agreement with available theoretical solutions. The benchmark validations indicated the ability of the proposed phase change model in several ways such as correct prediction of mass flow rate at phase interface, convergence toward the sharp interface limit, and ability to account for a thermal boundary layer in liquid-side of the phase interface. Additionally, no free parameter is defined considering the diffuse-interface nature of the LBE method such as a variable phase interface thickness for different density ratios or a variable time step in the definition of mass flow rate.

V. ACKNOWLEDGMENT

This work is supported by the U.S. NRC Faculty Development Grant and U.S. Department of Energy, Office of Nuclear Energys Nuclear Energy University Programs.

Appendix A: Proof of Eq. (20)

The proof of Eq. (20) introduced in [34] is shown in this appendix. This equation states,

$$\delta t \mathbf{e}_\alpha \cdot \nabla T = (\mathbf{n} \cdot \mathbf{e}_\alpha \delta t)(\mathbf{n} \cdot \nabla T). \tag{A1}$$

A two-dimensional case is considered here and extension to the three-dimensional form is straightforward. The involved vectors are expanded in Cartesian coordinates as $\mathbf{e}_\alpha = e_x\hat{\mathbf{i}} + e_y\hat{\mathbf{j}}$, $\mathbf{n} = n_x\hat{\mathbf{i}} + n_y\hat{\mathbf{j}}$, and $\nabla T = T_x\hat{\mathbf{i}} + T_y\hat{\mathbf{j}}$. Parameters T_x and T_y are temperature gradients in x and y directions, respectively. Expanding Eq. (A1) yields,

$$\left[e_x - n_x^2 e_x - n_x n_y e_y\right] T_x + \left[e_y - n_x n_y e_x - n_y^2 e_y\right] T_y = 0. \tag{A2}$$

The terms inside the square brackets should be zero in order to satisfy relation in Eq. (A2). Therefore,

$$\begin{bmatrix} 1 - n_x^2 & -n_x n_y \\ -n_x n_y & 1 - n_y^2 \end{bmatrix} \begin{bmatrix} e_x \\ e_y \end{bmatrix} = 0. \tag{A3}$$

The determinant of the coefficient matrix in Eq. (A3) should be zero to hold the relation in this equation valid,

$$\begin{vmatrix} 1 - n_x^2 & -n_x n_y \\ -n_x n_y & 1 - n_y^2 \end{vmatrix} = 1 - \left(n_x^2 + n_y^2\right) = 0. \tag{A4}$$

The equality in Eq. (A4) is fulfilled since $\mathbf{n}$ is a unit normal vector such that $|\mathbf{n}| = 1$. In general, the vector identity in Eq. (A1) is applicable for any non-zero vector (such as ∇T) as long as the $\mathbf{n}$ vector is a unit normal vector.

---

[1] V. P. Carey, *Liquid Vapor Phase Change Phenomena* (CRC Press, 2007).

[2] D. Juric and G. Tryggvason, Int. J. Multiphase Flow **24**, 387 (1998).

[3] S. W. J. Welch and J. Wilson, J. Comput. Phys. **160**, 662 (2000).

[4] B. Shu, F. Dammel, and P. Stephan, in *International Symposium on Advances in Computational Heat Transfer (CHT-08 ICHMT)* (Marrakech, Morocco, 2008).

[5] Y. Sato and B. Ničeno, J. Comput. Phys. **249**, 127 (2013).

[6] M. W. Akhtar and S. J. Kleis, Int. J. Multiphase Flow **53**, 88 (2013).

[7] G. Son and V. K. Dhir, J. Heat Transf. **120**, 183 (1998).

[8] X. Luo, M. J. Ni, A. Ying, and M. A. Abdou, Numer. Heat Tr. B-Fund. **48**, 425 (2005).

[9] F. Giboua, L. Chenb, D. Nguyenc, and S. Banerjeed, J. Comput. Phys. **222**, 536 (2007).

[10] A. Onuki, Phys. Rev. E **75**, 036304 (2007).

[11] K. Tsujimoto, A. Nakamura, T. Shakouchi, and T. Ando, in *7th International Conference on Multiphase Flow (ICMF-2010)* (Tampa, FL, 2010).

[12] R. Borcia and M. Bestehorn, Eur. Phys. J. B **44**, 101 (2005).

[13] A. Badillo, Phys. Rev. E **86**, 041603 (2012).

[14] Q. Li, Q. J. Kang, M. M. Francois, Y. L. He, and K. H. Luo, Int. J. Heat Mass Tran. **85**, 787 (2015).

[15] B. J. Palmer and D. R. Rector, Phys. Rev. E **61**, 5295 (2000).

[16] Z. Dong, W. Li, and Y. Song, Numer. Heat Tr. A-Appl. **55**, 381 (2009).

[17] A. Markus and G. Hazi, Phys. Rev. E **83**, 046705 (2011).

[18] H. Safari, M.H. Rahimian, and M. Krafczyk, Phys. Rev. E **88**, 013304 (2013).

[19] D. M. Anderson, G. B. McFadden, and A. A. Wheeler, Annu. Rev. Fluid. Mech. **30**, 139 (1998).

[20] X. He, S. Chen, and R. Zhang, J. Comput. Phys. **152**, 642 (1999).

[21] S. Farokhirad, J. F. Morris, and T. Lee, Phys. Fluids **27**, 102102 (2015).

[22] R. Zhang, S. Farokhirad, T. Lee, and J. Koplik, Phys. Fluids **26**, 082003 (2014).

[23] S. Farokhirad, T. Lee, and J. F. Morris, Commun. Comput. Phys. **13**, 706 (2013).

[24] V. Alexiades and A. Solomon, *Mathematical Modeling of Melting and Freezing Processes* (Hemisphere Publishing Corporation, 1993).

[25] T. Lee and C.-L. Lin, J. Comput. Phys. **206**, 16 (2005).

[26] T. Lee and P. F. Fischer, Phys. Rev. E **74**, 046709 (2006).

[27] H. Ding, P. Spelt, and C. Shu, J. Comput. Phys. **226**, 2078 (2007).

[28] O. Filippova and D. Hänel, J. Comput. Phys. **158**, 139 (2000).

[29] X. He and L.-S. Luo, Phys. Rev. E **55**, R6333 (1997).

[30] X. He, S. Chen, and G. Doolen, J. Comput. Phys. **146**, 282 (1998).

[31] L.-S. Luo, Phys. Rev. Lett. **81**, 1618 (1998).

[32] Y.-H. Qian and S.-Y. Chen, Phys. Rev. E **61**, 2712 (2000).

[33] D. Jacgmin, in *34th Aerospace Sciences Meeting* (Reno, NV, 1996).

[34] K. Connington and T. Lee, J. Comput. Phys. **250**, 601 (2013).

[35] G. Tauriello and P. Koumoutsakos, J. Comput. Phys. **283**, 388 (2015).

[36] M. K. Bowen and R. Smith, Proc. R. Soc. A **461**, 1975 (2005).

[37] X. Yang, X. Zhang, Z. Li, and G.-W. He, J. Comput. Phys. **228**, 7821 (2009).

[38] G. R. Guedon, Ph.D. thesis, Politecnico di Milano (2013).

[39] V. Babin and R. Holyst, J. Phys. Chem. B **109**, 11367 (2005).

[40] L. Scriven, Chem. Eng. Sci. **10**, 1 (1959).